Evolutionary conservation of centriole rotational asymmetry in the human centrosome

Noémie Gaudin [1], Paula Martin Gil [1], Meriem Boumendjel [1], Dmitry Ershov [2,3], Catherine Pioche-Durieu [1], Manon Bouix [1], Quentin Delobelle [1], Lucia Maniscalco [1], Thanh Bich Ngan Phan [1], Vincent Heyer [4,5,6,7], Bernardo Reina-San-Martin [4,5,6,7] and Juliette Azimzadeh [1,8].

[1] Université de Paris, CNRS, Institut Jacques Monod, 75006, Paris, France.

[2] Image Analysis Hub, C2RT, Institut Pasteur, Paris, France.

[3] Hub de Bioinformatique et Biostatistique – Département Biologie Computationnelle, Institut Pasteur, USR 3756 CNRS, Paris, France.

[4] Institut de Génétique et de Biologie Moléculaire et Cellulaire (IGBMC), Illkirch, France.

[5] Institut National de la Santé et de la Recherche Médicale (INSERM), U1258, Illkirch, France.

[6] Centre National de la Recherche Scientifique (CNRS), UMR7104, Illkirch, France.

[7] Université de Strasbourg, Illkirch, France.

[8] Author for correspondence: juliette.azimzadeh@ijm.fr

Keywords: centriole, centrosome, LRRCC1, VFL1, C2CD3, Joubert syndrome, asymmetry.

Abbreviations:

DA: distal appendage; JBTS: Joubert syndrome; MCC: multiciliated cell; PCM: pericentriolar material; SAG: SMOOTHENED agonist; SMO: SMOOTHENED; TZ: transition zone.

Abstract

Centrioles are formed by microtubule triplets in a nine-fold symmetric arrangement. In flagellated protists and in multiciliated cells, accessory structures tethered to specific triplets render the centrioles rotationally asymmetric, a property that is key to cytoskeletal and cellular organization in these contexts. In contrast, centrioles within the centrosome of animal cells display no conspicuous rotational asymmetry. Here, we uncover rotationally asymmetric molecular features in human centrioles. Using ultrastructure expansion microscopy, we show that LRRCC1, the ortholog of a protein originally characterized in flagellate green algae, associates preferentially to two consecutive triplets in the distal lumen of human centrioles. LRRCC1 partially co-localizes and affects the recruitment of another distal component, C2CD3, which also has an asymmetric localization pattern in the centriole lumen. Together, LRRCC1 and C2CD3 delineate a structure reminiscent of a filamentous density observed by electron microscopy in flagellates, termed the 'acorn'. Functionally, the depletion of LRRCC1 in human cells induced defects in centriole structure, ciliary assembly and ciliary signaling, supporting that LRRCC1 cooperates with C2CD3 to organizing the distal region of centrioles. Since a mutation in the *LRRCC1* gene has been identified in Joubert syndrome patients, this finding is relevant in the context of human ciliopathies. Taken together, our results demonstrate that rotational asymmetry is a conserved ancient property of centrioles. Our work also reveals that asymmetrically localized proteins are key for primary ciliogenesis and ciliary signaling in human cells.

46 **Introduction**

47

48 Centrioles are cylindrical structures with a characteristic ninefold symmetry, which results
49 from the arrangement of their constituent microtubule triplets (LeGuennec et al., 2021). In
50 animal cells, centrioles are essential for the assembly of centrosomes and cilia. The centrosome,
51 composed of two centrioles embedded in a pericentriolar material (PCM), is the main organizer
52 of the microtubule cytoskeleton. In addition, most vertebrate cells possess a primary cilium, a
53 sensory organelle that assembles from the oldest centriole within the centrosome, called mother
54 centriole (Kumar and Reiter, 2021).

55 Centrioles within the centrosome show no apparent rotational asymmetry, *i.e.,* no
56 structural asymmetry of the microtubule triplets. In vertebrates, the mother centriole carries
57 distal appendages (DAs) and subdistal appendages arranged in a symmetric manner around the
58 centriole cylinder (Kumar and Reiter, 2021). In contrast, the centriole/basal body complex of
59 flagellates, to which the animal centrosome is evolutionary related, is characterized by marked
60 rotational asymmetries (Azimzadeh, 2021; Yubuki and Leander, 2013). In flagellates, an array
61 of fibers and microtubules anchored asymmetrically at centrioles controls the spatial
62 organization of the cell (Feldman et al., 2007; Yubuki and Leander, 2013). The asymmetric
63 attachment of cytoskeletal elements appears to rely on molecular differences between
64 microtubule triplets. In the green alga *Chlamydomonas reinhardtii,* Vfl1p (Variable Flagella
65 number 1 protein) localizes principally at two triplets near the attachment site of a striated fiber
66 connecting the centrioles (Silflow et al., 2001). This fiber is absent or mispositioned in the *vfl1*
67 mutant, leading to defects in centriole position and number, and overall cytoskeleton
68 disorganization (Adams et al., 1985; Feldman et al., 2007). In the same region, a rotationally
69 asymmetric structure termed the 'acorn' was observed in the centriole lumen by transmission

electron microscopy. The acorn appears as a filament connecting five successive triplets and is in part colocalized with Vfl1p (Geimer and Melkonian, 2005, 2004).

We recently established that Vfl1p function is conserved in the multiciliated cells (MCCs) of planarian flatworms, which was later confirmed in xenopus (Basquin et al., 2019; Nommick et al., 2021). MCCs assemble large numbers of centriole that are polarized in the plane of the plasma membrane to enable the directional beating of the cilia (Meunier and Azimzadeh, 2016), like in *C. reinhardtii*. The planarian ortholog of Vfl1p is required for the assembly of two appendages that decorate MCC centrioles asymmetrically, the basal foot and the ciliary rootlet (Basquin et al., 2019). Depleting Vfl1p orthologs in planarian or xenopus MCCs alters centriole rotational polarity, reminiscent of the *vfl1* phenotype in *C. reinhardtii* (Adams et al., 1985; Basquin et al., 2019; Nommick et al., 2021). Intriguingly, the human ortholog of Vfl1p, called LRRCC1 (Leucine Rich Repeat and Coiled Coil containing 1) localizes at the centrosome despite the lack of rotationally asymmetric appendage in this organelle (Andersen et al., 2003; Muto et al., 2008). Furthermore, a homozygous mutation in the *LRRCC1* gene was identified in two siblings affected by a ciliopathy called Joubert syndrome (JBTS), suggesting that LRRCC1 might somehow affect the function of non-motile cilia (Shaheen et al., 2016).

Here, we show that LRRCC1 localizes in a rotationally asymmetric manner in the centrioles of the human centrosome. We further establish that LRRCC1 is required for proper ciliary assembly and signaling, which likely explains its implication in JBTS. LRRCC1 affects the recruitment at centrioles of another ciliopathy protein called C2CD3 (C2 domain containing 3), which we found to also localize in a rotationally asymmetric manner, forming a pattern reminiscent of the acorn described in flagellates. Our findings uncover the unanticipated rotational asymmetry of centrioles in the human centrosome and show that this property is connected to the assembly and function of primary cilia.

96 # Results

97

98 **LRRCC1 localizes asymmetrically at the distal end of centrioles**

99 To investigate a potential role of LRRCC1 at the centrosome, we first sought to determine its
100 precise localization at the centrosome. We raised antibodies against two different fragments
101 within the long C-terminal coiled-coil domain of LRRCC1 (Ab1, 2), which both stained the
102 centrosome region in human Retinal Pigmented Epithelial (RPE1) cells (Fig. 1a; Supplemental
103 Fig. S1b), as previously reported (Muto et al., 2008). Labeling intensity was decreased in
104 LRRCC1-depleted cells for both antibodies, supporting their specificity (Fig. 4a; Supplemental
105 Fig. S1c, e, f, h). LRRCC1 punctate labelling in the centrosomal region indicated that it is
106 present within centriolar satellites, confirming a previous finding that LRRCC1 interacts with
107 the satellite component PCM1 (Gupta et al., 2015). Importantly, following nocodazole
108 treatment to depolymerize microtubules, the satellites were dispersed but a fraction of LRRCC1
109 was retained at the centrioles (Fig. 1a; Supplemental Fig. S1b, e), supporting that LRRCC1 is
110 a core centriole component.

111 To determine LRRCC1 localization more precisely within the centriolar structure, we used
112 ultrastructure expansion microscopy (U-ExM) (Gambarotto et al., 2019) combined with
113 imaging on a Zeiss Airyscan 2 confocal microscope, thereby increasing the resolution by a
114 factor of ~ 8 compared to conventional confocal microscopy. We found that LRRCC1 localizes
115 at the distal end of centrioles as well as of procentrioles (Fig. 1b). Strikingly, and unlike any
116 other known centriole components, LRRCC1 decorated the distal end of centrioles in a
117 rotationally asymmetric manner. Indeed, LRRCC1 was detected close to the triplet blades and
118 towards the lumen of the centriole (Fig. 1c). The staining was often associated with two or
119 more consecutive triplets, one of them being usually more brightly labelled than the others. In
120 addition, a fainter staining was consistently detected along the entire length of all triplets (Fig.

121 1b, see brighter exposure). This pattern was observed in both RPE1 and HEK 293 cells and
122 was obtained with both anti-LRRCC1 antibodies (Supplemental Fig. S1g), supporting its
123 specificity. There was some variability in the distal pattern, particularly in the distance between
124 LRRCC1 and the centriole wall (Fig. 1c), which possibly resulted from the fact that the
125 centrioles were not perfectly orthogonal to the imaging plan. To obtain a more accurate picture
126 of LRRCC1 localization, we generated 3D reconstructions that we realigned, first along the
127 vertical axis, then with respect to one another using the most intense region of the LRRCC1
128 labelling as a reference point (Fig. 1d; Supplemental Fig. S2a-c). An average 3D reconstruction
129 was then generated (Fig. 1e) and revealed that in transverse view, LRRCC1 was mainly
130 associated to one triplet, and to a lesser extent to its direct neighbor counterclockwise, on their
131 luminal side. A longitudinal view confirmed that LRRCC1 is principally located at the distal
132 end of centrioles.

133 Together, our results show that LRRCC1 is localized asymmetrically within the distal
134 centriole lumen, establishing that centrioles within the human centrosome are rotationally
135 asymmetric.

136

137 **The localization pattern of LRRCC1 is similar at the centrosome and in mouse MCCs**

138 LRRCC1 orthologs are required for establishing centriole rotational polarity in planarian and
139 xenopus MCCs, like in *C. reinhardtii* (Basquin et al., 2019; Nommick et al., 2021; Silflow et
140 al., 2001). It is therefore plausible that LRRCC1-related proteins localize asymmetrically in
141 MCC centrioles, and indeed, Lrrcc1 was recently found associated to the ciliary rootlet in
142 xenopus MCCs (Nommick et al., 2021). To determine whether LRRCC1 also localizes at the
143 distal end of MCC centrioles in addition to its rootlet localization, and if so, whether LRRCC1
144 localization pattern resembles that observed at the centrosome, we analyzed mouse ependymal
145 and tracheal cells by U-ExM. In *in vitro* differentiated ependymal cells, the labelling generated

146 by the anti-LRRCC1 antibody was consistent with our observations in human culture cells.
147 Mouse Lrrcc1 localized asymmetrically at the distal end of centrioles, opposite to the side
148 where the basal foot is attached (Fig. 2a), as determined by staining the basal foot marker γ-
149 tubulin (Clare et al., 2014). Lrrcc1 was also present at the distal end of procentrioles forming
150 via either the centriolar or acentriolar pathways (*i.e.,* around parent centrioles or deuterosomes,
151 respectively) (Fig. 2b). We also examined tracheal explants, in which centrioles were docked
152 and polarized at the apical membrane in higher proportions (Fig. 2c). We obtained an average
153 image of Lrrcc1 labelling from 35 individual centrioles aligned using the position of the basal
154 foot as a reference point. This revealed that Lrrcc1 is principally located in the vicinity of 3
155 triplets located opposite the basal foot, to the right of basal foot main axis (triplet number 9, 1
156 and 2 on the diagram in Fig. 2d). Lrrcc1 was located farther away from the triplet wall than in
157 centrioles of the centrosome, but this was likely an effect of a deformation of the centrioles
158 (Fig. 2c, d) caused by the incomplete expansion of the underlying cartilage layer in tracheal
159 explants. In agreement, Lrrcc1 was located close to the triplets in ependymal cell monolayers,
160 which expand isometrically. Besides the distal centriole staining, we found no evidence that
161 Lrrcc1 is associated to the ciliary rootlet in mouse MCCs, unlike in xenopus. The Lrrcc1 pattern
162 in mouse MCCs was thus similar to the pattern observed at the human centrosome.
163 Together, these results show that LRRCC1 asymmetric localization is a conserved feature
164 of mammalian centrioles, presumably linked to the control of centriole rotational polarity and
165 ciliary beat direction in MCCs.
166

167 **Centriole rotational asymmetry is not linked to stereotypical patterns of procentriole**
168 **position and orientation during centriole duplication**

169 In *C. reinhardtii*, centriole rotational polarity and flagellar beat direction depend on the position
170 and orientation at which new centrioles arise during cell division. Reflecting the stereotypical

171 organization of centrioles and procentrioles in this species, Vfl1p is recruited early and at a
172 fixed position at the distal end of procentrioles (Fig.3a) (Geimer and Melkonian, 2004; Silflow
173 et al., 2001). We therefore wondered whether this mechanism might be somewhat conserved
174 in human cells, which could then explain the persistence of LRRCC1 asymmetric localization
175 despite the lack of asymmetric appendages or ciliary motility in these cells. We first analyzed
176 the timing of LRRCC1 incorporation into procentrioles. LRRCC1 was already present at an
177 early stage of centriole assembly, when the procentrioles were only about 100 nm in length and
178 70 nm in diameter (Fig. 3b, c). LRRCC1 was then detected during successive stages of
179 procentriole elongation, always localizing asymmetrically and distally (Fig. 3c), like in *C.*
180 *reinhardtii*. We then examined LRRCC1 localization in duplicating centrosomes by generating
181 3D-reconstructions of diplosomes (*i.e.,* orthogonal centriole pairs) from RPE1 and HEK 293
182 cells processed by U-ExM (Fig. 3d). We analyzed two parameters: the angle between LRRCC1
183 in the procentriole and the long axis of the parent centriole used as reference (Fig. 3d, LRRCC1
184 localization in procentrioles), and the angle between procentriole position and LRRCC1 in the
185 parent centriole (Fig. 3d, Procentriole position with respect to centriolar LRRCC1). We found
186 that LRRCC1 localization in procentrioles was more often aligned with the long axis of the
187 parent centriole in RPE1 cells (Fig. 3d, top left panel, quadrants Q1 and Q3, respectively), but
188 less so in HEK 293 cells (top right panel), in which the distribution was closer to a random
189 distribution. Thus, human procentrioles do not arise in a fixed orientation, unlike in flagellates.
190 Next, we analyzed the position of procentrioles with respect to centriolar LRRCC1 (bottom
191 panels). Based on current models, procentriole assembly is expected to occur at a random
192 position around parent centrioles in animal cells (Takao et al., 2019). Identification of LRRCC1
193 provided the first opportunity to directly test this model. In diplosomes from both RPE1 and
194 HEK 293 cells, the position of procentrioles with respect to LRRCC1 location in the parent
195 centriole was variable, confirming that the position at which procentrioles assemble is not

196 precisely controlled in human cells. Interestingly, however, the procentrioles were not
197 distributed in a completely random fashion either. Procentrioles were found in quadrant Q2
198 (45-135 degrees clockwise from LRRCC1 centroid) on average 4 times less often than in the
199 other quadrants, both in RPE1 and HEK 293 cells, suggesting that rotational polarity of the
200 parent centriole somehow impacts procentriole assembly.

201 Overall, these results nevertheless suggest that the conservation of centriole rotational
202 asymmetry in human cells is likely not linked to a role in centriole duplication.

203

204 **LRRCC1 is required for primary cilium assembly and ciliary signaling**

205 A previous report identified a homozygous mutation in a splice acceptor site of the *LRRCC1*
206 gene in two siblings diagnosed with JBTS (Shaheen et al., 2016), but how disruption of
207 LRRCC1 expression affects ciliary assembly and signaling has never been investigated. To
208 address this, we generated RPE1 cell lines deficient in LRRCC1 using two different
209 CRISPR/Cas9 strategies and targeting two different regions of the *LRRCC1* locus. We could
210 not recover null clones despite repeated attempts in RPE1 - both wild type and $p53^{-/-}$ (Izquierdo
211 et al., 2014), HEK 293 and U2-OS cells, suggesting that a complete lack of LRRCC1 is possibly
212 deleterious. Nevertheless, we obtained partially depleted mutant clones, including three RPE1
213 clones targeted in either exons 11-12 (clone 1.1) or exons 8-9 (clones 1.2 and 1.9). We could
214 not evaluate the overall decrease in LRRCC1 levels since the endogenous LRRCC1 protein
215 was not detected by Western blot (Supplemental Fig. S1a). However, we confirmed the
216 decrease in centrosomal LRRCC1 levels by immunofluorescence using the two different anti-
217 LRRCC1 antibodies, as well as by quantitative RT-PCR (Fig. 4a; Supplemental Fig. S1c-e).

218 Following induction of ciliogenesis, the proportion of ciliated cells was decreased in all
219 three mutant clones compared to control cells (Fig. 4b). We were unable to obtain stable RPE1
220 cell lines expressing myc- or GFP-tagged versions of LRRCC1, and transient overexpression

221 of LRRCC1 in wild-type cells led to a decrease in the proportion of ciliated cells, making
222 phenotype rescue experiments difficult to interpret. We therefore used RNAi as an independent
223 method to verify the specificity of ciliary defects observed in CRISPR clones. Targeting
224 LRRCC1 expression using two different siRNAs, we obtained a comparable decrease in
225 LRRCC1 levels and in the proportion of ciliated cells as in the CRISPR clones (Fig. 4c;
226 Supplemental Fig. S1f). Sensory ciliopathies like JBTS result to a large extent from defective
227 Hedgehog signaling (Romani et al., 2013). We determined the effect of LRRCC1-depletion on
228 Hedgehog signaling by measuring the ciliary accumulation of the activator SMOOTHENED
229 (SMO) upon induction of the pathway (Rohatgi et al., 2007). Depletion of LRRCC1 by either
230 CRISPR editing or RNAi led to a drastic decrease in SMO accumulation at the primary cilium
231 following induction of the Hedgehog pathway by SMO-agonist (SAG) (Fig. 4d, e), and reduced
232 expression of the target gene *PTCH1* (Supplemental Fig. S1g) (Goodrich et al., 1996).
233 Taken together, our results demonstrate that LRRCC1 is required for proper ciliary
234 assembly and signaling in human cells, further establishing its implication in JBTS.
235
236 **Depletion of LRRCC1 induces defects in centriole structure**
237 Mutations in distal centriole components can alter centriole length regulation or the assembly
238 of DAs, which both result in defective ciliogenesis (Reiter and Leroux, 2017; Sharma et al.,
239 2021). We used U-ExM to search for possible defects in centriole structure in LRRCC1-
240 depleted RPE1 cells. We measured centriole length in the two RPE1 CRISPR clones that
241 express the lowest levels of LRRCC1 (1.1 and 1.9). Centrioles were co-stained with anti-
242 acetylated tubulin and an antibody against the DA component CEP164 to differentiate mother
243 and daughter centrioles. We observed an increase in centriole length in clone 1.9 (Fig. 5a),
244 which expresses the lowest levels of LRRCC1, compared to control cells (483 ± 53 nm for
245 mother and 372 ± 55 nm for daughter centrioles in clone 1.9; 427 ± 56 nm for mother and 320

246 ± 46 nm for daughter centrioles in control cells; mean ± SD). Although on a limited sample
247 size, we also observed abnormally long centrioles by transmission electron microscopy in this
248 clone (494 ± 73 nm in clone 1.9, N = 9; 429 ± 52 nm in control cells, N = 3; mean ± SD) (Fig.
249 5b). However, clone 1.1 was not significantly different from control cells by U-ExM,
250 suggesting that this phenotype is not fully penetrant at the remaining levels of LRRCC1
251 expression observed in the CRISPR clones. We next used U-ExM to analyze the structure of
252 DAs labelled with anti-CEP164 antibody (Fig. 5c-e). In RPE1 control cells, 80 ± 14 % of
253 mother centriole had 9 properly shaped DAs, but this proportion fell to 57 ± 16 % and 44 ± 17
254 % (mean ± SD) in clones 1.1 and 1.9, respectively (Fig. 5c, d). Mutant clones exhibited an
255 increased proportion of centrioles with one or more abnormally shaped DAs (29 ± 17 % and
256 42 ± 18 % in clones 1.1 and 1.9, respectively, compared to 11 ± 11 % in control cells; mean ±
257 SD). We obtained similar results in a HEK 293 CRISPR clone expressing half the control levels
258 of LRRCC1 (Fig. 5e; Supplemental Fig. S1h). LRRCC1-depletion did not affect overall
259 CEP164 levels at mother centrioles in the CRISPR clones (Supplemental Fig. S3a, d),
260 consistent with the relatively mild defect in DA morphology observed by U-ExM.
261 Together, these results show that a partial loss of LRRCC1 leads to abnormal DA
262 morphology.
263
264 **LRRCC1 and C2CD3 delineate a rotationally asymmetric structure in human centrioles**
265 We next wanted to determine whether LRRCC1 cooperates with other distal centriole
266 components. Proteins shown to be recruited early at procentriole distal end include CEP290
267 (Kim et al., 2008), OFD1 (Singla et al., 2010) and C2CD3 (Thauvin-Robinet et al., 2014). Of
268 particular interest, OFD1 and C2CD3 are required for DA assembly and centriole length
269 control, and mutations in these proteins have been implicated in sensory ciliopathies (Singla et
270 al., 2010; Thauvin-Robinet et al., 2014; Tsai et al., 2019; Lei Wang et al., 2018). We first

271 determined whether depletion of LRRCC1 either by CRISPR editing or by RNAi led to
272 modifications in the recruitment of these proteins within centrioles. We found no major
273 differences in the centrosomal levels of OFD1 and CEP290 compared to control cells
274 (Supplemental Fig. S3b, c, e, f). In contrast, C2CD3 levels were moderately increased in cells
275 depleted from LRRCC1 either by CRISPR editing (clones 1.1 and 1.9) or by RNAi (Fig. 6a,
276 b). We thus analyzed C2CD3 further by U-ExM. As described previously, C2CD3 localized
277 principally at the distal extremity of centrioles (Fig. 6c) (Tsai et al., 2019; Yang et al., 2018).
278 Strikingly, the C2CD3 labelling was also asymmetric, both in terms of shape, often a C-shape,
279 and position within the centriole lumen (Fig. 5d). We next generated an average 3D
280 reconstruction of the C2CD3 pattern using the region where the C2CD3 signal is closest to the
281 centriole wall (after realignment along the vertical axis) as a reference point. This confirmed
282 that C2CD3 forms a C-shaped pattern – or possibly a ring-shaped pattern of uneven intensity,
283 positioned asymmetrically in the centriole lumen (Fig. 6e). To determine whether this
284 localization pattern is affected by LRRCC1-depletion, we analyzed C2CD3 in LRRCC1
285 CRISPR clones 1.1 and 1.9. The C2CD3 pattern was more variable than in control RPE1 cells,
286 and was often abnormal in shape, position, or both (Fig. 6f). As a result, averaging the signal
287 from 47 (1.1) or 24 (1.9) individual LRRCC1-depleted centrioles as previously produced
288 aberrant patterns, most strikingly in the clone expressing lower levels of LRRCC1 (clone 1.9;
289 Fig. 6g). Thus, LRRCC1 is required for the proper shape and asymmetric positioning of the
290 C2CD3-containing distal structure.

291 To determine whether LRRCC1 and C2CD3 might belong to a common structure, we next
292 examined the respective positions of C2CD3 and LRRCC1 within the centriole. We co-stained
293 centrioles with our anti-LRRCC1 antibody and a second anti-C2CD3 antibody produced in
294 sheep (Table 1). We confirmed that LRRCC1 and C2CD3 are present in the same distal region
295 of the centriole (Fig. 7a). In transverse views, the two proteins were usually not perfectly

colocalized but found in close vicinity of one another near the microtubule wall (Fig. 6e). However, C2CD3 distal staining was consistently fainter than with the previous antibody, and we either could not observe a full C-shaped pattern, or we could not image it due to fluorescence bleaching. Neither anti-C2CD3 antibodies worked in mouse, so we were not able to compare C2cd3 and Lrrcc1 localization in MCCs. Nevertheless, the results obtained by individually labelling LRRCC1 and C2CD3 at the centrosome (Fig. 1e, 6e, g) together with the co-localization data (Fig. 7a) are consistent with the hypothesis that LRRCC1 is located where the C2CD3-containing structure is closer to the centriole wall (Fig. 7b). C2CD3 was not co-immunoprecipitated with a GFP-LRRCC1 fusion protein however, suggesting that LRRCC1 and C2CD3 do not directly interact (Supplemental Fig. S4).

Taken together, our results support that C2CD3 localizes asymmetrically in the distal lumen of human centrioles, a pattern that depends in part on LRRCC1.

310 **Discussion**

311

312 Here, we show that centrioles within the human centrosome are rotationally asymmetric despite
313 the apparent nine-fold symmetry of their ultrastructure. This asymmetry is manifested by a
314 specific enrichment in LRRCC1 near two consecutive triplets, and the asymmetric localization
315 of C2CD3 within the centriole lumen. Depletion of LRRCC1 perturbed the asymmetric
316 recruitment of C2CD3 and induced defects in centriole structure, ciliogenesis and ciliary
317 signaling, supporting that LRRCC1 contributes to organizing the distal centriole region
318 together with C2CD3. LRRCC1 localizes like its *C. reinhardtii* ortholog Vfl1p, and C2CD3
319 delineates a filamentous structure reminiscent of the acorn described in this species (Geimer
320 and Melkonian, 2005, 2004) and in *Trypanosoma brucei* (Vaughan and Gull, 2016).
321 Collectively, our results support that rotational asymmetry is a conserved property of centrioles
322 linked to ciliary assembly and signaling in humans.

323

324 **LRRCC1 and C2CD3 belong to a conserved rotationally asymmetric structure**

325 Our work identifies two proteins located asymmetrically in the distal centriole lumen of the
326 human centrosome, each with a specific pattern. LRRCC1 localizes principally near two
327 consecutive triplets, with the first triplet counterclockwise labelled approximately 50 % more
328 than the next one. This pattern is highly reminiscent of the LRRCC1 ortholog Vfl1p, which
329 localizes predominantly to the triplet facing the second centriole (referred to as triplet 1), and
330 to a lesser extent to its immediate neighbor counterclockwise (triplet 2; Fig. 7b) (Silflow et al.,
331 2001). In *C. reinhardtii*, triplets 1 and 2 are positioned directly opposite to the direction of
332 flagellar beat, which is directed towards triplet 6 (Fig. 7b) (Lin et al., 2012). In mouse MCCs,
333 Lrrcc1 is associated to triplets located not exactly opposite to the basal foot but with a clockwise
334 shift of at least 20° from the basal foot axis. However, the beating direction was shown to be

335 also shifted approximately 20° clockwise relative to the position of the basal foot in bovine
336 tracheal MCCs (Schneiter et al., 2021) (Fig. 2d). The position of Lrrcc1/Vfl1p-labelled triplets
337 with respect to ciliary beat direction might thus be similar in *C. reinhardtii* and in animal
338 MCCs. Overall, the specific localization pattern of Vfl1p-related proteins at the distal end of
339 centrioles, and their requirement for centriole positioning and ciliary beat orientation when
340 motile cilia are present, appear to be conserved between flagellates and animals.

341 The second protein conferring rotational asymmetry to human centrioles, C2CD3, delineates
342 a C-shape positioned asymmetrically in the lumen. The localization of C2CD3 had been studied
343 before, including by super-resolution microscopy approaches, without this asymmetry being
344 noted (Tsai et al., 2019; Yang et al., 2018). This difference might result from the fact that we
345 corrected the vertical alignment of the centrioles prior to averaging multiple images. Several
346 lines of evidence support the hypothesis that the C2CD3-containing structure is homologous
347 to the acorn, a 10 nm-filament connecting five consecutive triplets along the centriole wall and
348 across the lumen in *C. reinhardtii* (Fig. 7b) (Geimer and Melkonian, 2004; Vaughan and Gull,
349 2016). First, the C2CD3 labelling is consistent with a circular filament. Second, the C2CD3-
350 containing structure is localized asymmetrically in the distal lumen in close vicinity of at least
351 three consecutive triplets. Third, C2CD3 is partially co-localized with LRRCC1 near the
352 microtubule wall. And last, C2CD3 orthologs are found in a variety of flagellated unicellular
353 eukaryotes, including the green alga *Micromonas pusilla* (Zhang and Aravind, 2012),
354 suggesting an ancestral association to centrioles and cilia. The partial co-localization of Vfl1p
355 and the acorn in *C. reinhardtii*, and the observation that both are already present at the distal
356 end of procentrioles, led to propose that Vfl1p might also be a component of the acorn (Geimer
357 and Melkonian, 2004). Consistent with this idea, both LRRCC1 and C2CD3 are recruited early
358 at the distal end of human procentrioles, and LRRCC1 is required for the proper recruitment
359 and/or positioning of the C2CD3-containing structure. C2CD3 recruitment at the centrioles

360 also depends on the proteins CEP120 and Talpid3 (Tsai et al., 2019), which possibly explains
361 why C2CD3 recruitment is not diminished, and is even increased in LRRCC1-depleted
362 centrioles. Future work will help deciphering the relationships between these different proteins
363 and characterize in more details the architecture of the rotationally asymmetric structure at the
364 distal end of mammalian centrioles.
365

366 **Rotationally asymmetric centriole components are required for ciliogenesis**

367 Our results uncover a link between centriole rotational asymmetry and primary ciliogenesis in
368 human cells. Mutations in C2CD3 have been involved in several sensory ciliopathies, including
369 JBTS (Boczek et al., 2018; Cortés et al., 2016; Ooi, 2015; Thauvin-Robinet et al., 2014). The
370 associated ciliary defects are likely caused by anomalies in the structure of centrioles, since
371 depleting C2CD3 inhibits centriole elongation and DA assembly, whereas C2CD3
372 overexpression leads to centriole hyper-elongation (Thauvin-Robinet et al., 2014; Wang et al.,
373 2018; Ye et al., 2014). We observed similar defects in LRRCC1-depleted cells, but of
374 comparatively lesser extent. Defects in DA morphology were observed in all CRISPR clones
375 analyzed, and centriole length was increased in the clone with the most severe phenotype. The
376 fact that LRRCC1-depletion has a more limited impact on centriole assembly than perturbation
377 of C2CD3 levels suggests that LRRCC1 might not be directly involved in centriole length
378 control or DA formation, however. The defects observed in LRRCC1-depleted cells could
379 instead result indirectly from the abnormal localization of C2CD3. Besides the defects in
380 centriole structure, it is likely that LRRCC1-depletion also perturbs the organization of the
381 ciliary gate, as LRRCC1-depleted cells exhibited a drastic reduction in Hedgehog signaling.
382 Loss of ciliary gate integrity interferes with the accumulation of SMO in the cilium upon
383 activation of the Hedgehog pathway and is a frequent consequence of ciliopathic mutations
384 (Garcia-Gonzalo and Reiter, 2017). The ciliary gate consists of the TZ and the DA region,

385 which both contribute to regulating protein trafficking in and out of the cilium (Garcia-Gonzalo
386 and Reiter, 2017; Nachury, 2018). The anomalies in DA morphology observed in LRRCC1-
387 depleted cells could disrupt the organization of the so-called DA matrix (Yang et al., 2018),
388 thus preventing SMO accumulation in the cilium. Another, non-mutually exclusive possibility
389 is that the architecture of the TZ, which forms directly in contact with the distal end of the
390 centriole, is altered by LRRCC1-depletion. In either case, our observations in RPE1 cells are
391 consistent with the JBTS diagnosis in two siblings carrying a mutation in the *LRRCC1* gene
392 (Shaheen et al., 2016), further establishing that *LRRCC1* is a novel ciliopathy gene. Besides
393 signaling, ciliary gate integrity is required for axoneme extension and indeed, LRRCC1-
394 depleted cells formed cilia at lower frequency than control cells – a defect that might also result
395 from perturbed DA architecture. In the *vfl1* mutant of *C. reinhardtii*, both unanchored
396 centrioles and centriole docked at the plasma membrane but lacking a flagellum were observed
397 (Adams et al., 1985). This would support that LRRCC1/Vfl1p requirement for properly
398 assembling the ciliary gate is a conserved functional aspect of this family of proteins (Fig. 7c).
399 Why is there a rotationally asymmetric structure at the base of primary cilia, and how does
400 this structure form and contribute to the assembly of the DAs and the cilium remain open
401 questions. In *C. reinhardtii* and in MCCs, LRRCC1 function is linked to the assembly of
402 asymmetric appendages, which must be correctly positioned in relation to ciliary beat direction
403 (Fig. 7c). An asymmetric structure present early during centriole assembly and ultimately
404 located near the cilium appears well suited for this task. The conservation of such a structure
405 at the base of the primary cilium could perhaps indicate that primary cilia also possess
406 rotationally asymmetric features, which would open interesting new perspectives on ciliary
407 roles in heath and disease.
408
409

410 **Other roles for centriole rotational assembly in human cells**

411 Our finding that procentrioles do not form completely at random with respect to LRRCC1
412 location in the parent centriole suggests that centriole rotational polarity can influence centriole
413 duplication in human cells. In *C. reinhartdtii*, procentrioles are formed at fixed positions with
414 respect to the parent centrioles, to which they are bound by a complex array of fibrous and
415 microtubular roots (Fig. 7c) (Geimer and Melkonian, 2004; Yubuki and Leander, 2013). The
416 process is likely different at the centrosome since the roots typical of flagellates are not
417 conserved in animal cells (Azimzadeh, 2021; Yubuki and Leander, 2013). In mammalian cells,
418 procentrioles form near the wall of the parent centriole following the recruitment of early
419 centriole proteins directly to the PCM components CEP152 and CEP192 (Yamamoto and
420 Kitagawa, 2021). It is nonetheless conceivable that an asymmetry in triplet composition could
421 result in local changes in PCM composition, which in turn could negatively impact PLK4
422 activation in this region. For instance, our analyses in planarian MCCs led us to postulate that
423 linkers might be tethered to one side of the centrioles in a VFL1-dependent manner and
424 independently of centriole appendages (Basquin et al., 2019). Future work will allow
425 deciphering how centriole rotational asymmetry influences centriole duplication, and whether
426 it affects other aspects of centriole positioning and cellular organization.

427

428 **Acknowledgements**

429 The authors are deeply grateful to Marine Laporte, Virginie Hamel, Paul Guichard and Davide
430 Gambarotto for teaching them the U-ExM procedure and for sharing antibodies; Arnaud
431 Echard and Takashi Ochi for critical reading of the manuscript; Amélie-Rose Boudjema and
432 Alice Meunier for providing mouse ependymal cells and Isabelle Le Parco for the tracheal
433 tissue; Juliane Da Graça and Simon Herman for technical help; Rémi Le Borgne for help with
434 transmission electron microscopy and for critical reading of the manuscript. We acknowledge

the core imaging facility of Institut Jacques Monod (ImagoSeine facility, member of the France BioImaging infrastructure supported by grant ANR-10-INBS-04 from the French National Research Agency). This work was supported by La Ligue Contre le Cancer and Fondation ARC pour la recherche sur le cancer funding to J.A. N.G. was recipient of a MESRI PhD fellowship from the French Government and a 4th year PhD fellowship from the Fondation pour la Recherche Médicale.

Declaration of interests

The authors declare no competing interests.

445 # Material and Methods

446

447 **Cell culture**

448 RPE1 cells (hTERT-RPE1, RRID:CVCL_4388) were cultured in DMEM/F-12 medium
449 (ThermoFisher Scientific) supplemented with 10 % fetal calf serum (ThermoFisher Scientific),
450 100 U/mL penicillin and 100 µg/mL streptomycin (ThermoFisher Scientific). Ciliogenesis was
451 induced by culturing RPE1 cells in medium without serum during 48 hours. HEK 293 cells
452 (kind gift from F. Causeret, Institut Imagine, Paris) were cultured in DMEM medium
453 (ThermoFisher Scientific) supplemented with 10 % fetal calf serum and antibiotics as
454 previously. All cells were kept at 37°C in the presence of 5 % CO_2.

455

456 **Mouse ependymal cells and tracheal tissue**

457 All experiments were performed in accordance with French Agricultural Ministry and
458 European guidelines for the care and use of laboratory animals. *In vitro* differentiated
459 ependymal cells were a kind gift from A.R. Boudjema and A. Meunier (IBENS, Paris). They
460 were prepared as described previously (Delgehyr et al., 2015; Mercey et al., 2019) from
461 Cen2GFP mice (CB6-Tg(CAG-EGFP/CETN2)3-4Jgg/J, The Jackson Laboratory). The
462 fragment of trachea was obtained from a wild-type mouse of the Swiss background (kindly
463 provided by I. Le Parco, Institut Jacques Monod).

464

465 **CRISPR/Cas9 editing**

466 LRRCC1 mutant clones were obtained by two different CRISPR/Cas9 strategies. First, RPE1
467 cells were co-transfected with plasmid px154-1 (U6p-gRNA#1_U6p-gRNA#2_CMVpnCas9-
468 EGFP_SV40p-PuroR-pA with gRNA#1: 5'- AGA ATT CTA CCC TAC CTG CGG - 3' and
469 gRNA#2: 5'- TAA GGT AGT GCT TCC TAC CGG -3') targeting the *LRRCC1* locus in exon

470 8, and px155-24 (U6p-gRNA#3_U6p-gRNA#4_CMVpnCas9-mCherry_SV40p-PuroR-pA;
471 gRNA#1: 5'- ATC TAC TCG GAA AGC TGA CGG -3' and 5'- GCT TGA GGG CTC AAA
472 TAC CGG - 3') targeting exon 9. Both constructs express the nickase mutant of Cas9 fused to
473 either EGFP or mCherry. Two days after transfection, EGFP- and mCherry-positive cells were
474 sorted by flow cytometry and grown at low concentration. Individual clones were picked after
475 2 weeks and analyzed by PCR to detect short insertions/deletions. A single clone was obtained
476 (clone 1.1), which was further characterized by genomic sequencing. Both alleles of *LRRCC1*
477 contained deletions (~ 0.6 kb deletion of exon 9 and a ~1.5 kb deletion of exon 8) leading to
478 frameshifts. In a second approach, cells were co-transfected using a mix of 3 CRISPR/Cas9
479 Knockout Plasmids (sc-413781; Santa Cruz Biotechnology) targeting exons 11 (5'- CTT GTT
480 CTC TTT CTC GAT GAA GG – 3' and 5' - ACT TCT TGC ATT GAA AGA ACA GG - 3')
481 or 12 (5' - CGT GTT AAG CCA GCA GTA TAT GG – 3') of *LRRCC1,* together with the
482 corresponding Homology Directed Repair plasmids carrying a puromycine-resistance cassette
483 (sc-413781-HDR; Santa Cruz Biotechnology), following the recommendations of the
484 manufacturer. Mutant clones were selected by addition of 2 µg/mL puromycine in the culture
485 medium and further screened by immunofluorescence.
486

487 **Inducible HEK 293 cell lines**

488 LRRCC1 full-length coding sequence was amplified from cDNA clone IMAGE:5272572
489 (Genbank accession: BC070092.1), corresponding to the longest isoform of LRRCC1
490 (NM_033402.5), after correction of a frameshift error by PCR mutagenesis. As N- and C-
491 terminal GFP fusions were not targeted to the centrosome, we inserted the GFP tag within the
492 LRRCC1 sequence in disordered regions present between the leucine rich repeat and coiled-
493 coil domains, either after amino acid 251 or 402. The fusions were cloned into the pCDNA-
494 5FRT (ThermoFischer Scientific) vector using the Gibson assembly method (Gibson et al.,

495 2009) and then integrated into the Flp-In-293 cell line using the Flp-In system (ThermoFischer
496 Scientific). Expression of the GFP-LRRCC1 fusions was induced by culturing the Flp-In-293
497 cell lines overnight in medium supplemented with 1 µ/mL doxycycline (ThermoFischer
498 Scientific).
499
500 **RNAi**
501 Ready to use double-stranded siRNA LRRCC1-si1 (target sequence: 5'- AAG GAG AAA
502 GAT GGA GAC GAT - 3') (Muto et al., 2008), LRRCC1-si2 (target sequence: 5'- TTA GAT
503 GAC CAA ATT CTA CAA - 3') and control siRNA (AllStars Negative Control) were
504 purchased from Qiagen. siRNAs were delivered into cells using Lipofectamine RNAiMAX
505 diluted in OptiMEM medium (ThermoFisher Scientific). Cells were fixed after 48 hours and
506 processed for immunofluorescence. For RNAi-depletion of ciliated cells, RPE1 cells grown in
507 complete culture medium were treated by RNAi, incubated for 2 days, then submitted to a
508 second round of RNAi. After 8 hours, cells were washed 3 x in PBS then cultured during 24
509 hours in serum-free medium to induce ciliogenesis.
510
511 **qRT-PCR**
512 Total RNA extracts were obtained using the Nucleospin RNA kit (Macherey-Nagel) and
513 cDNAs were synthetized using SuperScript III reverse transcriptase (Thermofisher Scientific).
514 qPCR was performed with the GoTaq qPCR Master Mix (Promega) in a LightCycler 480
515 instrument (Roche) using the primers listed in Table 2. Quantification of relative mRNA levels
516 was performed using CHMP2A and EMC7 as reference genes following the MIQE guidelines
517 (Bustin et al., 2009).
518
519

520 **Antibodies**

521 Fragments encoding either aa 671-805 (Ab1) or aa 961-1032 (Ab2) of LRRCC1
522 (NP_208325.3) were cloned in pGST-Parallel1 and expressed in *Escherichia coli.* The GST-
523 fusion proteins were purified under native conditions using glutathione agarose (ThermoFisher
524 Scientific) and the LRRCC1 fragments were recovered by Tev protease cleavage and dialyzed
525 before rabbit immunization (Covalab). Antibodies were affinity-purified over the
526 corresponding GST-LRRCC1 fusion bound to Affi-Gel 10 resin (Bio-Rad). Other primary and
527 secondary antibodies used in this study are listed in Table 1.

528

529 **Western blot**

530 For whole-cell extracts, Flp-In-293 cell lines expressing the GFP-LRRCC1 fusions were
531 induced overnight with doxycycline, collected by centrifugation, and resuspended in Western
532 blot sample buffer prior to incubation at 95 °C for 5 minutes. For immunoprecipitation
533 experiments, doxycycline-induced cells expressing LRRCC1 with a GFP inserted after aa 402
534 were resuspended in lysis buffer (50 mM Tris pH 8, 150 mM NaCl, 1 % NP-40, 0.5 % sodium
535 deoxycholate, 0.1 % SDS) supplemented with 1 mM $MgCl_2$, 20 µg/mL DNAse I (Roche) and
536 a protease inhibitor cocktail (Complete mini, EDTA-free, Roche). After 30 minutes on ice, the
537 lysates were centrifuged at 15 000 g for 10 minutes at 4°C. The supernatants were then
538 incubated with Dynabeads M-280 sheep-anti rabbit magnetic beads (ThermoFischer Scientific)
539 previously incubated with rabbit anti-IgGs, either anti-GFP or anti-HA tag for the control IP
540 (Table 1), and rotated for 3 hours at 4°C. After 3 washes with lysis buffer, immunoprecipitated
541 proteins were recovered by resuspending the beads in sample buffer and heating at 95 °C for 5
542 minutes. The samples were then run on 4-20% Mini-Protean TGX precast protein gels (Bio-
543 Rad) and transferred onto PVDF membrane using the iBlot 2 blot system (ThermoFischer
544 Scientific). The membranes were blocked and incubated with antibodies following standard

545 procedures, then visualized using Pierce ECL plus chemiluminescence reagents
546 (ThermoFischer Scientific) on an ImageQuant LAS 4000 camera system (GE Healthcare Life
547 Sciences).
548
549 **Immunofluorescence**
550 Cells were fixed in cold methanol for 5 minutes at – 20 °C, blocked 10 minutes with 3 % BSA
551 (Sigma Aldrich) in PBS containing 0.05 % Tween-20 (PBST-0.05%), then incubated with
552 primary antibodies diluted in PBST-0.05% containing 3 % BSA for 1 hour. After washing 3 x
553 1 minute in PBST-0.05%, cells were incubated 2 hours with secondary antibodies in PBST-
554 0.05% containing 3 % BSA and 5 µg/mL Hoechst 33342 (ThermoFischer Scientific), washed
555 in PBST-0.05% as previously, and mounted using Fluorescence Mounting Medium (Agilent).
556 For staining of primary cilia with anti-acetylated tubulin, cells were incubated 2 hours on ice
557 prior to methanol fixation. For quantification of SMO accumulation within cilia, confluent cells
558 cultured during 24 hours in serum-free medium were supplemented with 200 nM SAG (Sigma)
559 diluted in DMSO, or DMSO alone for 24 hours. Cells were then co-stained for SMO and
560 ARL13B to determine the position of the primary cilium. For all experiments involving
561 induction of ciliogenesis by serum deprivation, we verified that cells were arrested in G0 by
562 immunofluorescence staining of Ki67. To visualize centriolar LRRCC1, and to quantify
563 CEP290 centrosomal levels, cells were treated during 1 hour with 5 µM nocodazole prior to
564 fixation. Images were acquired using an Axio Observer Z.1 microscope (Zeiss) equipped with
565 a sCMOS Orca Flash4 LT camera (Hamamatsu) and a 63x objective (Plan Apo, N.A. 1.4). The
566 structured illumination microscopy (SIM) image was acquired on an ELYRA PS.1 (Zeiss)
567 equipped with an EMCCD iXon 885 camera (Andor) and a 63x objective (Plan Apo, N.A. 1.4).
568
569

570 **Ultrastructure expansion microscopy**

571 We used the U-ExM protocol described in (Gambarotto et al., 2019) with slight modifications.
572 Cells grown on glass coverslips were incubated in a fresh solution of 1 % acrylamide and 0.7
573 % formaldehyde diluted in PBS. After incubating 5 hours to overnight at 37 °C, the coverslips
574 were washed with PBS and placed cells down on a drop of 35 µL monomer solution (19.3 %
575 sodium acrylate, 10 % acrylamide, 0.1 % bis-acrylamide in PBS) to which 0.5 % TEMED and
576 0.1 % ammonium persulfate were added just before use. The coverslips were incubated 5
577 minutes on ice then 1 hour at 37°C, then transferred to denaturation buffer (200 mM SDS, 200
578 mM NaCl, 50 mM Tris pH9) for 15 minutes with agitation to detach the gels from the
579 coverslips. The gels were then incubated in denaturation buffer 1.5 hours at 95 °C, washed 2 x
580 30 minutes in deionized water then incubated overnight in water at room temperature to allow
581 expansion of the gel. The gels were measured at this step to determine the coefficient of
582 expansion. After 2 x 10 minutes in PBS, the gels were cut into smaller pieces then incubated 3
583 hours at 37 °C with primary antibodies diluted in saturation buffer (3 % BSA, 0.05 % Tween-
584 20 in PBS). The gel fragments were then washed 3 x 10 minutes in PBST-0.1%, incubated 3 h
585 with secondary antibodies and washed in PBST-0.1% as previously. Finally, the gels were
586 incubated 2 x 30 minutes in de-ionized water then left to expand overnight in de-ionized water
587 to regain their maximum size. For U-ExM of mouse tracheal cells, a fragment of WT mouse
588 trachea (kind gift from I. Le Parco, IJM, Paris) was adhered on a poly-lysine coated coverslip
589 then processed as described above with the following modifications: for the first step, the
590 fragment of trachea was incubated overnight to 48 hours in 1 % acrylamide and 0.7 %
591 formaldehyde in PBS; they were placed 15 min on ice prior to the 1-hour incubation at 37 °C
592 and the transfer to denaturation buffer. Note that GFP fluorescence was quenched during U-
593 ExM processing, so the GFP-Cen2 construct expressed in ependymal cells was not detectable
594 in final samples. Gels were imaged on Lab-Tek chamber slides (0.15 mm) coated with poly-

595 lysine (ThermoFisher Scientific). Images were acquired at room temperature using either a
596 LSM780 confocal microscope (Zeiss) equipped with an oil 63x objective (Plan Apo, N.A. 1.4),
597 or an LSM980 confocal microscope with Airyscan 2 (Zeiss) equipped with an oil 63x objective
598 (Plan Apo, N.A. 1.4).
599
600 **Image analysis**
601 Protein levels were determined using ImageJ software (Schneider et al., 2012) by measuring
602 the fluorescence intensity in the centrosome or cilium area and subtracting the cytoplasmic
603 background in z-series taken at 0.5-µm interval.
604 To generate average images of LRRCC1 and C2CD3, U-ExM samples were systematically
605 imaged using Airyscan 2. Only centrioles that were nearly perpendicular to the imaging plane
606 were acquired in order to maximize the resolution in transverse views. Calculating the average
607 image consisted of several steps: cropping out individual centrioles, aligning them, providing
608 reference points, standardizing centrioles using the reference points, and averaging
609 (Supplemental Fig. S2). The cropping was done in ImageJ, and for aligning and providing the
610 reference points a graphical user interface was developed based on Napari (Sofroniew et al.,
611 2020). Centriole alignment: the direction of centriole long axis was selected manually and used
612 to position the centriole vertically. Providing the reference points: 9 points were manually
613 selected to outline the circle of microtubules triplets and the location of the protein of interest.
614 The centriole was also framed in Z dimension with a rectangle. Standardization: the reference
615 points were used to calculate all necessary transformations (rotation, scaling and translation)
616 to map the original image of a centriole to the standard image. Averaging: an average image
617 was calculated for all the successive XY planes of the standardized image stacks. For alignment
618 of tracheal cell centrioles, since the current version of the graphical user interface can only
619 accommodate two channels, the position of the basal foot provided by the γ-tubulin channel

620 was reported manually in the acetylated tubulin channel using Image J. The images were then
621 processed as before using the manual annotation as a reference point for the basal foot.
622 For analysis of procentriole position and LRRCC1 location in procentrioles, 3D-
623 reconstructions of diplosomes processed for U-ExM were obtained using IMARIS software
624 (Oxford Instruments).
625
626 **Electron microscopy**
627 RPE1 cells were grown at confluence before induction of ciliogenesis for 72 hours by serum
628 deprivation. Cells were fixed 30 minutes in 2.5 % glutaraldehyde (Electron Microscopy
629 Sciences), 2 % paraformaldehyde (Electron Microscopy Sciences), 1 mM $CaCl_2$ in PBS, then
630 washed 3 x 5 minutes in PBS. Samples were then post-fixed during 30 minutes in 1 % Osmium
631 tetroxide (Electron Microscopy Sciences), then washed 3 x 5 minutes in water. Dehydration
632 was performed using graded series of ethanol in water for 5 minutes 30%, 50%, 70%, 90%,
633 100%, 100%. Resin infiltration was performed by incubating 30 minutes in an Agar low
634 viscosity resin (Agar Scientific Ltd) and EtOH (1:2) mix, then 30 minutes in a resin and EtOH
635 (2:1) mix followed by overnight incubation in pure resin. The resin was then changed and the
636 samples further incubated during 1.5 hours prior to inclusion in gelatin capsules and overnight
637 polymerization at 60 °C. 70 nm sections were obtained using an EM UC6 ultramicrotome
638 (Leica), post-stained in 4 % aqueous uranyl acetate and lead citrate, and observed at 80 kV
639 with a Tecnai12 transmission electron microscope (ThermoFischer Scientific) equipped with a
640 1K×1K Keen View camera (OSIS).
641
642 **Statistical analysis**
643 All statistical analyses were performed using the Prism7 for Mac OS X software (GraphPad
644 Software, Inc.). All values are provided as mean ± SD. The number of experimental replicates

645 and the statistical test used are indicated in the figure legends, and the p values are included
646 when statistically different.
647
648

649 **References**

650

651 Adams GM, Wright RL, Jarvik JW. 1985. Defective temporal and spatial control of flagellar
652 assembly in a mutant of Chlamydomonas reinhardtii with variable flagellar number. *J Cell*
653 *Biol* **100**:955–964.
654 Azimzadeh J. 2021. Evolution of the centrosome, from the periphery to the center. *Current*
655 *Opinion in Structural Biology* **66**:96–103. doi:10.1016/j.sbi.2020.10.020
656 Basquin C, Ershov D, Gaudin N, Vu HT, Louis B, Papon JF, Orfila AM, Mansour S, Rink JC,
657 Azimzadeh J. 2019. Emergence of a Bilaterally Symmetric Pattern from Chiral
658 Components in the Planarian Epidermis. *Dev Cell* **51**:516-525 e5.
659 doi:10.1016/j.devcel.2019.10.021
660 Boczek NJ, Hopp K, Benoit L, Kraft D, Cousin MA, Blackburn PR, Madsen CD, Oliver GR,
661 Nair AA, Na J, Bianchi DW, Beek G, Harris PC, Pichurin P, Klee EW. 2018.
662 Characterization of three ciliopathy pedigrees expands the phenotype associated with
663 biallelic C2CD3 variants. *European Journal of Human Genetics* **26**:1797–1809.
664 doi:10.1038/s41431-018-0222-3
665 Bustin SA, Benes V, Garson JA, Hellemans J, Huggett J, Kubista M, Mueller R, Nolan T,
666 Pfaffl MW, Shipley GL, Vandesompele J, Wittwer CT. 2009. The MIQE guidelines:
667 minimum information for publication of quantitative real-time PCR experiments. *Clin*
668 *Chem* **55**:611–622. doi:10.1373/clinchem.2008.112797
669 Clare DK, Magescas J, Piolot T, Dumoux M, Vesque C, Pichard E, Dang T, Duvauchelle B,
670 Poirier F, Delacour D. 2014. Basal foot MTOC organizes pillar MTs required for
671 coordination of beating cilia. *Nature communications* **5**:4888. doi:10.1038/ncomms5888
672 Cortés CR, McInerney-Leo AM, Vogel I, Rondón Galeano MC, Leo PJ, Harris JE, Anderson
673 LK, Keith PA, Brown MA, Ramsing M, Duncan EL, Zankl A, Wicking C. 2016.

674 Mutations in human C2CD3 cause skeletal dysplasia and provide new insights into
675 phenotypic and cellular consequences of altered C2CD3 function. *Scientific Reports* **6**.
676 doi:10.1038/srep24083
677 Delgehyr N, Meunier A, Faucourt M, Grau MB, Strehl L, Janke C, Spassky N. 2015.
678 Ependymal cell differentiation, from monociliated to multiciliated cells. *Methods in Cell*
679 *Biology* **127**:19–35. doi:10.1016/bs.mcb.2015.01.004
680 Feldman JL, Geimer S, Marshall WF. 2007. The mother centriole plays an instructive role in
681 defining cell geometry. *PLoS Biol* **5**:e149.
682 Gambarotto D, Zwettler FU, le Guennec M, Schmidt-Cernohorska M, Fortun D, Borgers S,
683 Heine J, Schloetel JG, Reuss M, Unser M, Boyden ES, Sauer M, Hamel V, Guichard P.
684 2019. Imaging cellular ultrastructures using expansion microscopy (U-ExM). *Nature*
685 *Methods* **16**:71–74. doi:10.1038/s41592-018-0238-1
686 Garcia-Gonzalo FR, Reiter JF. 2017. Open Sesame: How Transition Fibers and the Transition
687 Zone Control Ciliary Composition. *Cold Spring Harb Perspect Biol* **9**.
688 doi:10.1101/cshperspect.a028134
689 Geimer S, Melkonian M. 2005. Centrin scaffold in Chlamydomonas reinhardtii revealed by
690 immunoelectron microscopy. *Eukaryot Cell* **4**:1253–1263.
691 Geimer S, Melkonian M. 2004. The ultrastructure of the Chlamydomonas reinhardtii basal
692 apparatus: identification of an early marker of radial asymmetry inherent in the basal
693 body. *J Cell Sci* **117**:2663–2674.
694 Gibson DG, Young L, Chuang RY, Venter JC, Hutchison CA, Smith HO. 2009. Enzymatic
695 assembly of DNA molecules up to several hundred kilobases. *Nature Methods* **6**:343–345.
696 doi:10.1038/nmeth.1318

697 Goodrich L v., Johnson RL, Milenkovic L, McMahon JA, Scott MP. 1996. Conservation of the
698 hedgehog/patched signaling pathway from flies to mice: Induction of a mouse patched
699 gene by Hedgehog. *Genes and Development* **10**:301–312. doi:10.1101/gad.10.3.301
700 Gupta GD, Coyaud É, Gonçalves J, Mojarad BA, Liu Y, Wu Q, Gheiratmand L, Comartin D,
701 Tkach JM, Cheung SWT, Bashkurov M, Hasegan M, Knight JD, Lin ZY, Schueler M,
702 Hildebrandt F, Moffat J, Gingras AC, Raught B, Pelletier L. 2015. A Dynamic Protein
703 Interaction Landscape of the Human Centrosome-Cilium Interface. *Cell* **163**:1484–1499.
704 doi:10.1016/j.cell.2015.10.065
705 Izquierdo D, Wang WJ, Uryu K, Tsou MF. 2014. Stabilization of cartwheel-less centrioles for
706 duplication requires CEP295-mediated centriole-to-centrosome conversion. *Cell Rep*
707 **8**:957–965. doi:10.1016/j.celrep.2014.07.022
708 Kim J, Krishnaswami SR, Gleeson JG. 2008. CEP290 interacts with the centriolar satellite
709 component PCM-1 and is required for Rab8 localization to the primary cilium. *Hum Mol*
710 *Genet* **17**:3796–3805. doi:10.1093/hmg/ddn277
711 Kumar D, Reiter J. 2021. How the centriole builds its cilium: of mothers, daughters, and the
712 acquisition of appendages. *Current Opinion in Structural Biology*.
713 doi:10.1016/j.sbi.2020.09.006
714 LeGuennec M, Klena N, Aeschlimann G, Hamel V, Guichard P. 2021. Overview of the
715 centriole architecture. *Current Opinion in Structural Biology* **66**:58–65.
716 doi:10.1016/j.sbi.2020.09.015
717 Lin J, Heuser T, Song K, Fu X, Nicastro D. 2012. One of the Nine Doublet Microtubules of
718 Eukaryotic Flagella Exhibits Unique and Partially Conserved Structures. *PLoS ONE* **7**.
719 doi:10.1371/journal.pone.0046494

720 Mercey O, al Jord A, Rostaing P, Mahuzier A, Fortoul A, Boudjema AR, Faucourt M, Spassky
721 N, Meunier A. 2019. Dynamics of centriole amplification in centrosome-depleted brain
722 multiciliated progenitors. *Scientific Reports* **9**:1–11. doi:10.1038/s41598-019-49416-2
723 Meunier A, Azimzadeh J. 2016. Multiciliated cells in animals. *Cold Spring Harbor*
724 *Perspectives in Biology* **8**. doi:10.1101/cshperspect.a028233
725 Muto Y, Yoshioka T, Kimura M, Matsunami M, Saya H, Okano Y. 2008. An evolutionarily
726 conserved leucine-rich repeat protein CLERC is a centrosomal protein required for spindle
727 pole integrity. *Cell Cycle* **7**:2738–2748.
728 Nachury M v. 2018. The molecular machines that traffic signaling receptors into and out of
729 cilia. *Current Opinion in Cell Biology*. doi:10.1016/j.ceb.2018.03.004
730 Nommick A, Boutin C, Rosnet O, Bazellières E, Thomé V, Loiseau E, Viallat A, Kodjabachian
731 L. 2021. Lrrcc1 and Ccdc61 are conserved effectors of multiciliated cell function. *bioRxiv*
732 2021.01.30.428946. doi:10.1101/2021.01.30.428946
733 Ooi J. 2015. Mutations in C2CD3 cause oral-facial-digital syndrome through deregulation of
734 centriole length. *Clinical Genetics* **87**:328–329. doi:10.1111/cge.12545
735 Reiter JF, Leroux MR. 2017. Genes and molecular pathways underpinning ciliopathies. *Nat*
736 *Rev Mol Cell Biol* **18**:533–547. doi:10.1038/nrm.2017.60
737 Rohatgi R, Milenkovic L, Scott MP. 2007. Patched1 regulates hedgehog signaling at the
738 primary cilium. *Science* **317**:372–376. doi:10.1126/science.1139740
739 Romani M, Micalizzi A, Valente EM. 2013. Joubert syndrome: congenital cerebellar ataxia
740 with the molar tooth. *Lancet neurology* **12**:894–905. doi:10.1016/S1474-4422(13)70136-
741 4
742 Schneiter M, Halm S, Odriozola A, Mogel H, Rička J, Stoffel MH, Zuber B, Frenz M, Tschanz
743 SA. 2021. Multi-scale alignment of respiratory cilia and its relation to mucociliary
744 function. *Journal of Structural Biology* **213**:107680. doi:10.1016/j.jsb.2020.107680

745 Shaheen R, Szymanska K, Basu B, Patel N, Ewida N, Faqeih E, al Hashem A, Derar N, Alsharif
746 H, Aldahmesh MA, Alazami AM, Hashem M, Ibrahim N, Abdulwahab FM, Sonbul R,
747 Alkuraya H, Alnemer M, al Tala S, Al-Husain M, Morsy H, Seidahmed MZ, Meriki N,
748 Al-Owain M, AlShahwan S, Tabarki B, Salih MA, Ciliopathy W, Faquih T, El-Kalioby
749 M, Ueffing M, Boldt K, Logan C v, Parry DA, al Tassan N, Monies D, Megarbane A,
750 Abouelhoda M, Halees A, Johnson CA, Alkuraya FS. 2016. Characterizing the morbid
751 genome of ciliopathies. *Genome biology* **17**:242. doi:10.1186/s13059-016-1099-5
752 Sharma A, Olieric N, Steinmetz MO. 2021. Centriole length control. *Current Opinion in*
753 *Structural Biology* **66**:89–95. doi:10.1016/j.sbi.2020.10.011
754 Silflow CD, LaVoie M, Tam LW, Tousey S, Sanders M, Wu W, Borodovsky M, Lefebvre PA.
755 2001. The Vfl1 Protein in Chlamydomonas localizes in a rotationally asymmetric pattern
756 at the distal ends of the basal bodies. *J Cell Biol* **153**:63–74.
757 Singla V, Romaguera-Ros M, Garcia-Verdugo JM, Reiter JF. 2010. Ofd1, a human disease
758 gene, regulates the length and distal structure of centrioles. *Dev Cell* **18**:410–424.
759 Sofroniew N, Lambert T, Evans K, Nunez-Iglesias J, Yamauchi K, Solak AC, Bokota G,
760 ziyangczi, Buckley G, Winston P, Tung T, Pop DD, Hector, Freeman J, Bussonnier M,
761 Boone P, Royer L, Har-Gil H, Axelrod S, Rokem A, Bryant, Kiggins J, Huang M, Vemuri
762 P, Dunham R, Manz T, jakirkham, Wood C, Siqueira A de, Chopra B. 2020. napari/napari:
763 0.3.8rc1. doi:10.5281/ZENODO.4046812
764 Takao D, Yamamoto S, Kitagawa D. 2019. A theory of centriole duplication based on self-
765 organized spatial pattern formation. *Journal of Cell Biology* **218**:3537–3547.
766 doi:10.1083/JCB.201904156
767 Thauvin-Robinet C, Lee JS, Lopez E, Herranz-Pérez V, Shida T, Franco B, Jego L, Ye F,
768 Pasquier L, Loget P, Gigot N, Aral B, Lopes CAM, St-Onge J, Bruel AL, Thevenon J,
769 González-Granero S, Alby C, Munnich A, Vekemans M, Huet F, Fry AM, Saunier S,

770 Rivière JB, Attié-Bitach T, Garcia-Verdugo JM, Faivre L, Mégarbané A, Nachury M v.
771 2014. The oral-facial-digital syndrome gene C2CD3 encodes a positive regulator of
772 centriole elongation. *Nature Genetics* **46**:905–911. doi:10.1038/ng.3031
773 Tsai JJ, Hsu W bin, Liu JH, Chang CW, Tang TK. 2019. CEP120 interacts with C2CD3 and
774 Talpid3 and is required for centriole appendage assembly and ciliogenesis. *Scientific*
775 *Reports* **9**. doi:10.1038/s41598-019-42577-0
776 Vaughan S, Gull K. 2016. Basal body structure and cell cycle-dependent biogenesis in
777 Trypanosoma brucei. *Cilia*. doi:10.1186/s13630-016-0023-7
778 Wang Lei, Failler M, Fu W, Dynlacht BD. 2018. A distal centriolar protein network controls
779 organelle maturation and asymmetry. *Nature Communications* **9**. doi:10.1038/s41467-
780 018-06286-y
781 Wang L, Failler M, Fu W, Dynlacht BD. 2018. A distal centriolar protein network controls
782 organelle maturation and asymmetry. *Nature communications* **9**:3938.
783 doi:10.1038/s41467-018-06286-y
784 Yamamoto S, Kitagawa D. 2021. Emerging insights into symmetry breaking in centriole
785 duplication: updated view on centriole duplication theory. *Current Opinion in Structural*
786 *Biology*. doi:10.1016/j.sbi.2020.08.005
787 Yang TT, Chong WM, Wang WJ, Mazo G, Tanos B, Chen Z, Tran TMN, Chen Y de, Weng
788 RR, Huang CE, Jane WN, Tsou MFB, Liao JC. 2018. Super-resolution architecture of
789 mammalian centriole distal appendages reveals distinct blade and matrix functional
790 components. *Nature Communications* **9**:1–11. doi:10.1038/s41467-018-04469-1
791 Ye X, Zeng H, Ning G, Reiter JF, Liu A. 2014. C2cd3 is critical for centriolar distal appendage
792 assembly and ciliary vesicle docking in mammals. *Proceedings of the National Academy*
793 *of Sciences of the United States of America* **111**:2164–2169.
794 doi:10.1073/pnas.1318737111

795 Yubuki N, Leander BS. 2013. Evolution of microtubule organizing centers across the tree of
796 eukaryotes. *The Plant journal : for cell and molecular biology* **75**:230–244.
797 doi:10.1111/tpj.12145
798 Zhang D, Aravind L. 2012. Novel transglutaminase-like peptidase and C2 domains elucidate
799 the structure, biogenesis and evolution of the ciliary compartment. *Cell Cycle* **11**:3861–
800 3875. doi:10.4161/cc.22068
801
802

803 **Figure legends**

804

805 **Figure 1. LRRCC1 is localized in a rotationally asymmetric manner at the distal end of**
806 **centrioles in the human centrosome. a)** LRRCC1 localization in non-treated RPE1 cells
807 (left) or in cells treated with nocodazole to disperse the pericentriolar satellites (right).
808 LRRCC1 (Ab2, yellow), γ-tubulin (PCM, magenta) and DNA (cyan). Bar, 5 µm (insets, 2 µm).
809 **b)** Longitudinal view of centrioles and procentrioles in the duplicating centrosome of an RPE1
810 cell analyzed by U-ExM. LRRCC1 (Ab2, yellow), acetylated tubulin (magenta). Bar, 0.5 µm.
811 **c)** Centrioles from WT RPE1 cells as seen from the distal end. LRRCC1 (Ab2, yellow),
812 acetylated tubulin (magenta). Bar, 0.2 µm. **d)** Workflow for calculating the average staining
813 from 3D-reconstructed individual centrioles generated from confocal z-stacks. The brightest
814 part of LRRCC1 signal was used as a reference point to align the centrioles. **e)** Average
815 LRRCC1 staining obtained from 34 individual centrioles viewed from the distal end, in
816 transverse and longitudinal views. A diagram representing the average pattern in transverse
817 view is also included.

818

819 **Figure 2. The LRRCC1 rotationally asymmetric pattern is conserved in mouse MCCs.**
820 **a)** Centrioles in the cytoplasm of mouse ependymal cells differentiating *in vitro* analyzed by
821 U-ExM, in longitudinal and transverse view. Lrrcc1 (Ab2, yellow), γ-tubulin (basal foot cap,
822 cyan) and acetylated tubulin (magenta). Of note, γ-tubulin was also detected in the proximal
823 lumen of centrioles. Bar, 0.2 µm. **b)** Procentrioles assembling via the centriolar (right) or the
824 deuterosome pathway (left and center) in ependymal cells. Lrrcc1 (Ab2, yellow), acetylated
825 tubulin (magenta). Bar, 0.2 µm. **c)** Transverse view of centrioles docked at the apical membrane
826 in fully differentiated mouse tracheal cells, viewed from the distal end. Lrrcc1 (Ab2, yellow),
827 γ-tubulin (cyan) and acetylated tubulin (magenta). Bar, 0.2 µm. **d)** Average image generated

828 from 35 individual centrioles from mouse trachea, viewed from the distal end, shown in
829 transverse and longitudinal views. The position of the basal foot (cyan dotted line) stained with
830 γ-tubulin was used as a reference point to align the centrioles. A diagram of the average pattern
831 in transverse view is shown, in which the direction of ciliary beat (Schneiter et al., 2021) is
832 represented by a dotted arrow and the basal foot axis by a green line. Triplets are numbered
833 counterclockwise from the LRRCC1 signal.
834
835 **Figure 3. The conservation of centriole rotational asymmetry in humans is not linked to**
836 **stereotypical patterns of procentriole position and orientation. a)** Early stage of
837 procentriole assembly stained for LRRCC1 (Ab2, yellow), SAS-6 (cyan) and acetylated tubulin
838 (magenta) in a HEK 293 cell. The brightness of the acetylated tubulin labelling was increased
839 in the inserts. Bar, 0.1 µm. **b)** Successive stages of centriole elongation in HEK 293 cells
840 stained for LRRCC1 (Ab2, yellow) and acetylated tubulin (magenta). Bar, 0.1 µm. **c)** Location
841 of LRRCC1 in the procentrioles (top panels) and position of the procentriole relative to its
842 parent centriole polarity (bottom panels), in RPE1 and HEK 293 centrioles analyzed by U-
843 ExM. For each diplosome, the angle between LRRCC1 in the procentriole and the centriole
844 long axis (top panels), or between the procentriole and LRRCC1 in the centriole (bottom
845 panels) was measured. The number of diplosomes analyzed is indicated. p values are indicated
846 when statistically different from a random distribution (χ^2-test).
847
848 **Figure 4. LRRCC1 is required for ciliary assembly and signaling. a)** Left: LRRCC1
849 staining (Ab2) of WT or LRRCC1-defficient RPE1 cells obtained by CRISPR/Cas9 editing
850 (clones 1.1, 1.2 and 1.9). Bar, 2 µm. Right: quantification of fluorescence intensity. Bars, mean
851 ± SD, 3 independent experiments. p values are provided when statistically significant from the
852 corresponding control (One-way ANOVA). **b)** Percentage of ciliated cells in WT or LRRCC1-

853 deficient serum-deprived cells. Bars, mean ± SD, ≥ 331 cells from 4 independent experiments
854 for each condition. p values are provided when statistically significant from the corresponding
855 control (One-way ANOVA). **c)** Percentage of ciliated cells in serum deprived RPE1 cells
856 treated with control or LRRCC1 siRNAs. Bars, mean ± SD, ≥ 83 cells from 3 independent
857 experiments for each condition. p values are provided when statistically significant from the
858 corresponding control (One-way ANOVA). **d)** Left: SMO (yellow) accumulation at primary
859 cilia (ARL13B, magenta) following SAG-induction of the Hedgehog pathway, in WT or
860 CRISPR RPE1 cells. Bar, 2 µm. Right: quantification of ciliary SMO expressed as a percentage
861 of the SAG-treated WT mean. Bars, mean ± SD, 3 independent experiments. p values are
862 provided when statistically significant from the corresponding control (One-way ANOVA). **e)**
863 Ciliary SMO expressed as a percentage of the SAG-induced WT mean in RPE1 cells treated
864 with control or LRRCC1 siRNAs. Bars, mean ± SD, 3 independent experiments. p values are
865 provided when statistically significant from the corresponding control (One-way ANOVA).
866
867 **Figure 5. Depleting LRRCC1 induces defects in centriole structure. a)** Centriole length in
868 mother (MC) and daughter (DC) centrioles analyzed by U-ExM in WT or LRRCC1-deficient
869 clones (1.1 and 1.9). Left: Centrioles were stained for acetylated tubulin (magenta) and CEP164
870 (yellow) to measure centriole length (arrows). Bar, 0.5 µm. Right: Quantification from 3
871 independent experiments. p values are provided when statistically significant from the
872 corresponding control (One-way ANOVA). **b)** Transmission electron microscopy view of
873 centrioles in WT and CRISPR (clone 1.9) RPE1 cells. Note that the two 1.9 centrioles are from
874 the same cell. Bar, 0.5 µm. **c)** Examples of normal DAs, DAs with abnormal morphology
875 (white arrowhead: abnormal spacing between consecutive DAs; cyan arrowhead: abnormal DA
876 shape) or missing DAs (grey arrowhead) analyzed by U-ExM. Bar, 1 µm. **d)** Percentages of
877 centrioles presenting DA defects in WT or CRISPR RPE1 cells. ≥ 87 centrioles from 8

878 independent experiments for each condition. p values are provided when statistically
879 significant from the corresponding control (Two-way ANOVA). **e)** Percentages of centrioles
880 presenting DA defects in WT or CRISPR HEK 293 (clone 21) cells. ≥ 40 centrioles from 4
881 independent experiments for each condition. p values are provided when statistically
882 significant from the corresponding control (Two-way ANOVA).
883
884 **Figure 6. C2CD3 localizes asymmetrically at the distal end of centrioles and is affected**
885 **by LRRCC1-depletion. a)** C2CD3 levels at the centrosome of WT or LRRCC1 CRISPR
886 RPE1 clones. Bars, mean ± SD, 3 independent experiments. p values are provided when
887 statistically significant from the corresponding control (One-way ANOVA). **b)** C2CD3 levels
888 at the centrosome in RPE1 cells treated with control or LRRCC1 siRNAs. Bars, mean ± SD, 3
889 independent experiments. p values are provided when statistically significant from the
890 corresponding control (One-way ANOVA). **c)** Longitudinal view of a centriole analyzed by U-
891 ExM and stained for C2CD3 (yellow) and acetylated tubulin (magenta). Bar, 0.2 µm. **d)**
892 Centrioles from WT RPE1 cells as viewed from the distal end. C2CD3 (yellow), acetylated
893 tubulin (magenta). Bar, 0.2 µm. **e)** Average C2CD3 staining obtained from 40 individual
894 centrioles from WT RPE1 cells viewed from the distal end, in transverse and longitudinal
895 views. The region where the C2CD3 signal is closest to the triplet wall after correction of
896 centriole orientation was used as a reference point to align the individual centrioles. A diagram
897 of the average pattern in transverse view is included. **f)** Centrioles from LRRCC1-deficient
898 cells (CRISPR clones 1.1 and 1.9) in transverse section as viewed from the distal end. C2CD3
899 (yellow), acetylated tubulin (magenta). Bar, 0.2 µm. **g)** Average C2CD3 staining obtained from
900 47 (clone 1.1) or 24 (clone 1.9) individual centrioles from LRRCC1-deficient RPE1 cells
901 viewed from the distal end, in transverse and longitudinal views.
902

903 **Figure 7. C2CD3 and LRRCC1 partially colocalize at the distal end of centrioles. a)** RPE1
904 centrioles processed for U-ExM and stained for LRRCC1 (Ab2, yellow), C2CD3 (cyan) and
905 acetylated tubulin (magenta). Bar, 0.1 µm. **b)** Model showing the possible location of LRRCC1
906 and C2CD3 relative to each other within human centrioles. Right panel: diagram showing the
907 respective positions of the acorn (Geimer and Melkonian, 2004) and Vfl1p (Silflow et al., 2001)
908 in *C. reinhardtii*. The direction of the flagellar beat is indicated by a dotted arrow, and the distal
909 striated fiber is in grey. **c)** Evolution of the roles played by Vfl1p/LRRCC1 proteins and
910 associated rotationally asymmetric centriolar substructures. In *C. reinhardtii*, Vfl1p is required
911 for proper ciliary assembly (1), as well as for the formation of fibers and microtubular roots (2)
912 that control the position of centrioles and procentrioles (3), and overall cellular organization
913 (Adams et al., 1985; Silflow et al., 2001). In human cells, LRRCC1 and C2CD3 are required
914 for primary cilium assembly (1) - this study and (Thauvin-Robinet et al., 2014; Ye et al., 2014)
915 - and a role in asymmetric anchoring of centrosome or cytoskeletal components might also be
916 conserved (2).
917
918 **Supplemental material**
919 **Fig. S1** provides additional data on LRRCC1 expression in CRISPR clones and RNAi-treated
920 cells. **Fig. S2** presents the image analysis pipeline for generating the average images of
921 LRRCC1 and C2CD3 staining. **Fig. S3** shows the quantification of the DA component
922 CEP164, and the distal centriole components CEP290 and OFD1, at the centrosome of RPE1
923 cells depleted from LRRCC1 by CRISPR or RNAi. **Fig. S4** shows that C2CD3 is not co-
924 immunoprecipitated with GFP-LRRCC1.
925

Table 1. Antibodies used in this study.

Antibody	Dilution IF	Dilution U-ExM	Dilution WB	RRID Identifier	Source	Reference
Primary antibodies						
Goat anti-ARL13B	1:100	/	/	RRID:AB_2058502	Santa Cruz Biotechnology	sc-102318
Guinea pig anti-alpha tubulin AA344 monobody	/	1:500	/		Geneva antibody facility	scFv-S11B
Guinea pig anti-beta tubulin AA345 monobody	/	1:500	/		Geneva antibody facility	scFv-F2C
Mouse anti-acetylated tubulin (6-11B-1)	1:1000	1:500	/	RRID:AB_628409	Santa Cruz Biotechnology	sc-23950
Mouse anti-CEP290 (B-7)	1:500	/	/	RRID:AB_2890036	Santa Cruz Biotechnology	sc-390462
Mouse anti-CBY (8-2)	1:500	/	/	RRID:AB_1561972	Santa Cruz Biotechnology	sc-101551
Mouse anti-gamma tubulin (GTU88)	1:2000	1:200	/	RRID:AB_532292	Sigma-Aldrich	T5326
Mouse anti-SAS-6	/	1:100	/	RRID:AB_1128357	Santa Cruz Biotechnology	sc-81431
Mouse anti-Smoothened	1:200	/	/	RRID:AB_1270802	Abcam	ab72130
Rabbit anti-ARL13B	1:500	/	/	RRID:AB_2060867	Proteintech	17711-1-AP
Rabbit anti-C2CD3	1:500	1:500	/	RRID:AB_10669542	Sigma-Aldrich	HPA038552
Rabbit anti-C2CD3	/	/	1:1000	RRID:AB_2718714	ThermoFisher Scientific	PA5-72860
Rabbit anti-CEP164	1:500	1:300	/	RRID:AB_2651175	Proteintech	22227-1-AP
Rabbit anti-GFP	/	/	1:1000	RRID:AB_591816	MBL International	598
Rabbit anti-HA	/	/	1:1000	RRID:AB_631618	Santa Cruz Biotechnology	sc-805
Rabbit anti-KI67	1:1000	/	/	RRID:AB_443209	Abcam	ab15580
Rabbit anti-LRRCC1 Ab1	1:500	1:200	/		This study	
Rabbit anti-LRRCC1 Ab2	1:500	1:300	1:1000		This study	
Rabbit anti-OFD1	1:500	/	/	RRID:AB_2890033.	Sigma-Aldrich	ABC961
Sheep anti-C2CD3	1:200	1:100	/	RRID:AB_10997138	R&D systems	AF7348
Secondary antibodies						
Donkey Anti-Goat IgG H&L (Alexa Fluor® 488)	1:500	1:500	/	RRID:AB_2687506	Abcam	ab150129
Donkey Anti-Goat IgG H&L (Alexa Fluor® 568)	1:500	1:500	/	RRID:AB_2636995	Abcam	ab175474
Donkey Anti-Goat IgG H&L (Alexa Fluor® 647)	1:500	1:100	/	RRID:AB_2732857	Abcam	ab150131
Donkey Anti-Mouse IgG H&L (Alexa Fluor® 488)	1:500	1:500	/	RRID:AB_2732856	Abcam	ab150105
Donkey Anti-Mouse IgG H&L (Alexa Fluor® 568)	1:500	1:500	/	RRID:AB_2636996	Abcam	ab175472
Donkey Anti-Mouse IgG H&L (Alexa Fluor® 647)	1:500	1:100	/	RRID:AB_2890037	Abcam	ab150107
Donkey Anti-Rabbit IgG H&L (Alexa Fluor® 488)	1:500	1:500	/	RRID:AB_2636877	Abcam	ab150073
Donkey Anti-Rabbit IgG H&L (Alexa Fluor® 647)	1:500	1:500	/	RRID:AB_2752244	Abcam	ab150075
Donkey Anti-Sheep IgG H&L (Alexa Fluor® 647)	/	1:100	/	RRID:AB_2884038	Abcam	ab150179
Goat Anti-Guinea Pig IgG (H+L) (Alexa Fluor 568)	/	1:100	/	RRID:AB_141954	ThermoFisher Scientific	A-11075
Goat Anti-Rabbit IgG (H+L) Horseradish Peroxidase Conjugate	/	/	1:1000	RRID:AB_2536530	ThermoFisher Scientific	G-21234

Table 2. PCR primers used in this study.

Primer	Sequence
LRRCC1-1_Fw	CAA CAA GGA TCT TCT CTA GCC CA
LRRCC1-1_Rv	AGT TTG GTC GTC TAT GAT TTT GCA
LRRCC1-2_Fw	GCA CAA CAA GGA TCT TCT CTA GC
LRRCC1-2_Rv	TCG CAG ACA TTC ATT CTC TCT AGA
PTCH1_Fw	CCC CTG TAC GAA GTG GAC ACT CTC
PTCH1_Rv	AAG GAA GAT CAC CAC TAC CTT GGC T
CHMP2A_Fw	ATG GGC ACC ATG AAC AGA CAG
CHMP2A_Rv	TCT CCT CTT CAT CTT CCT CAT CAC
EMC7_Fw	GTC AGA CTG CCC TAT CCT CTC C
EMC7_Rv	CAT GTC AGG ATC ACT TGT GTT GAC

Gaudin *et al.*

Figure 1

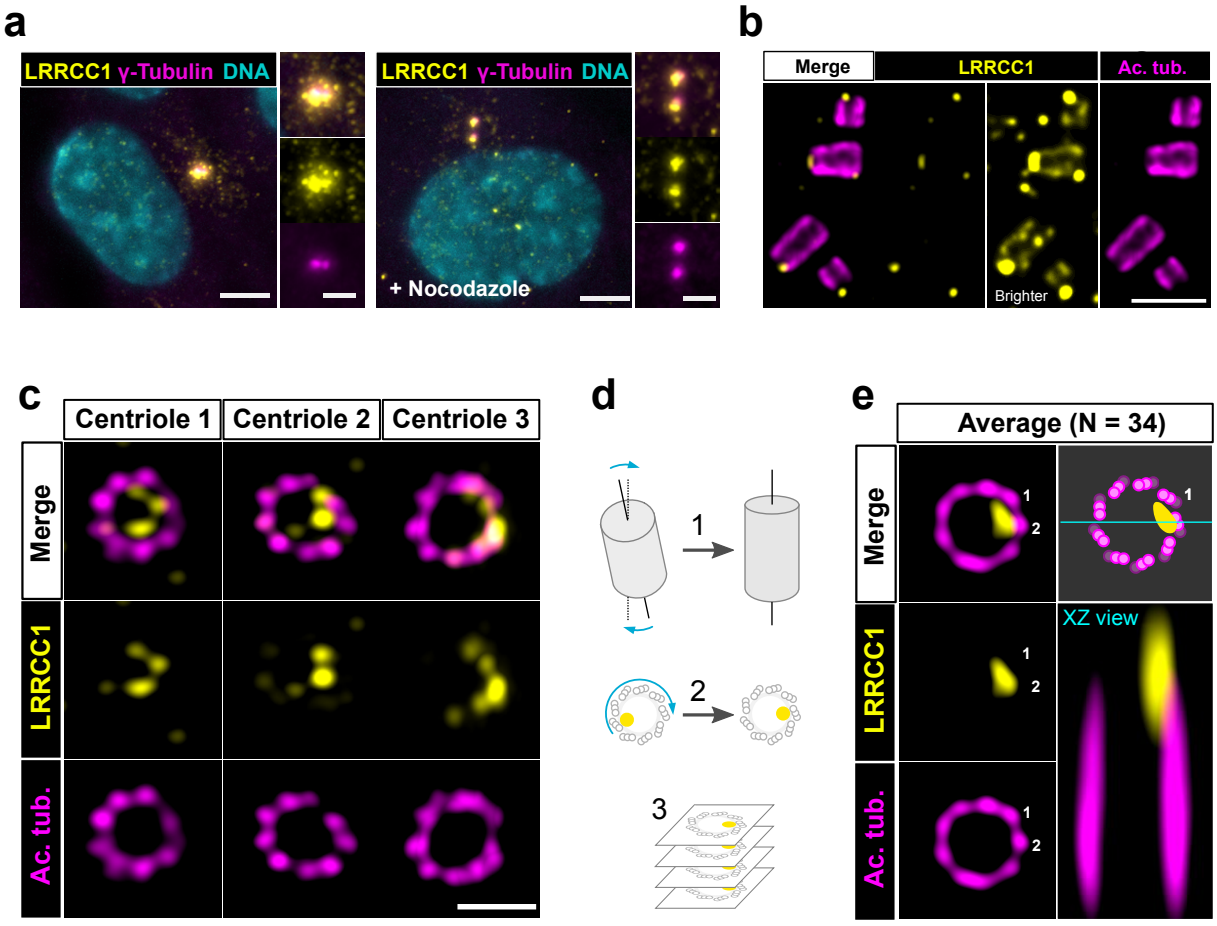

Figure 2

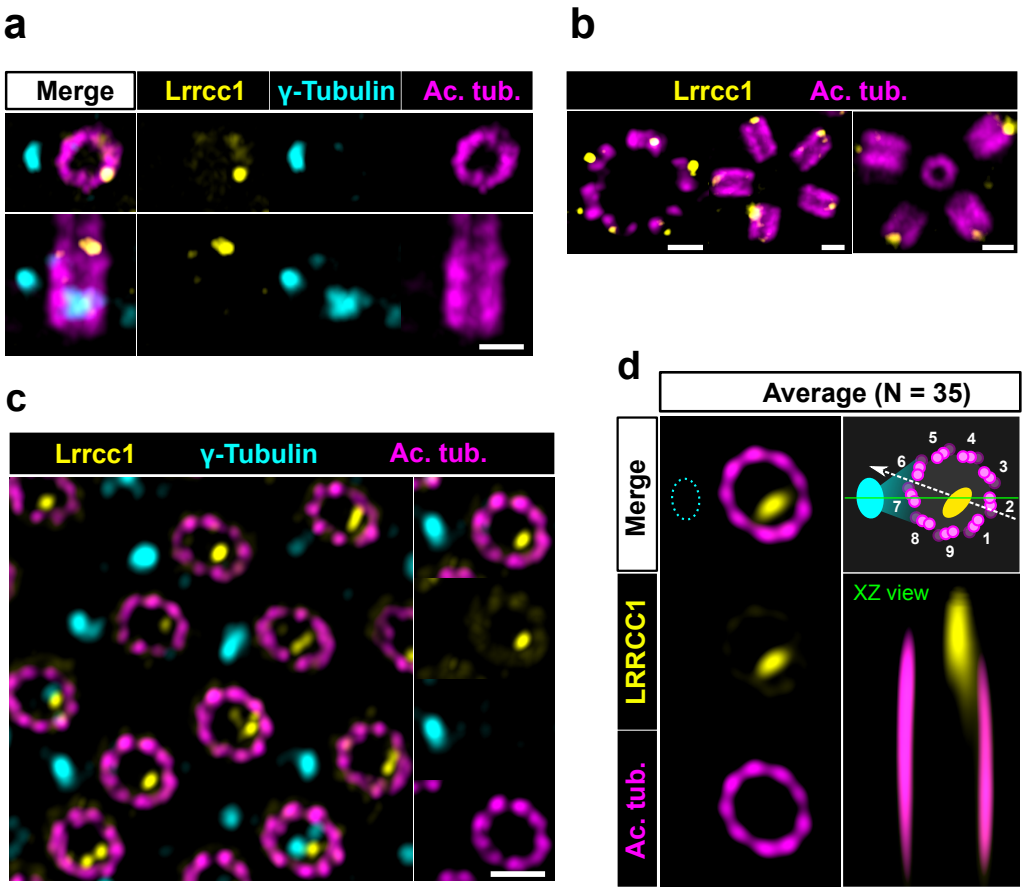
a
Merge
Lrrcc1
γ-Tubulin
Ac. tub.
b
Lrrcc1
Ac. tub.
c
Lrrcc1
γ-Tubulin
Ac. tub.
d
Average (N = 35)
Merge
LRRCC1
Ac. tub.
5
4
6
3
7
2
8
1
9
XZ view

Figure 3

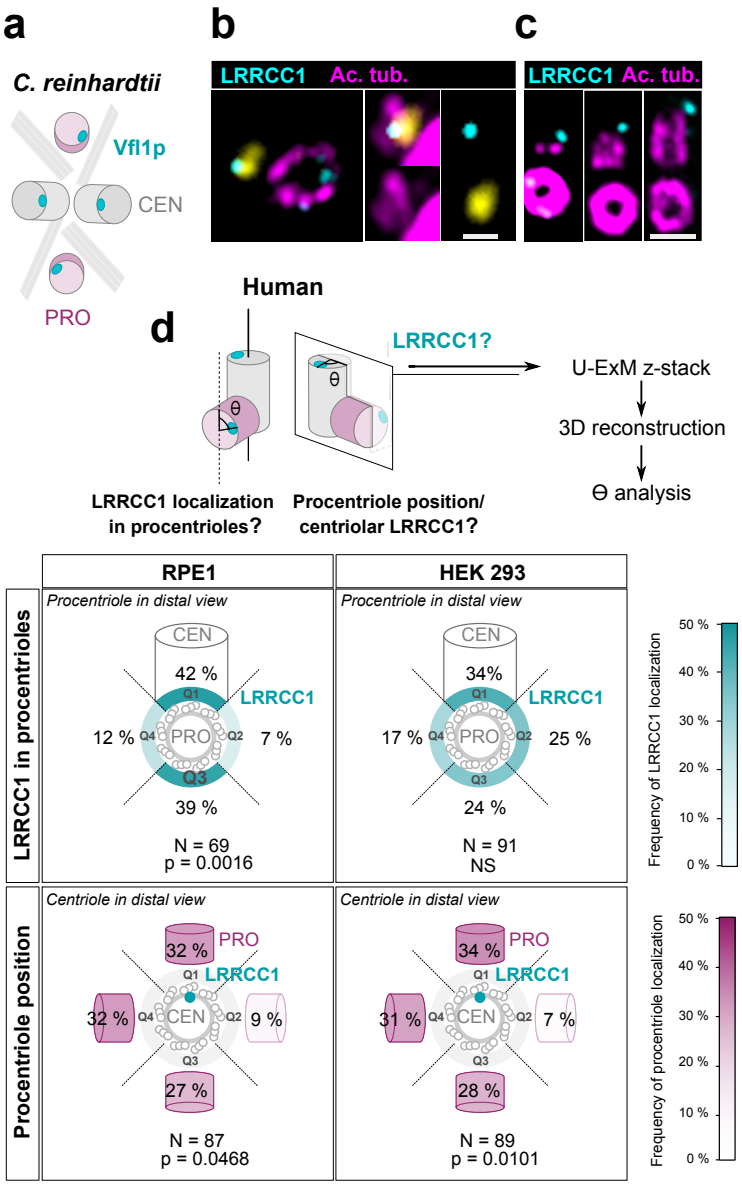
a
C. reinhardtii
Vfl1p
CEN
PRO
b
LRRCC1 Ac. tub.
c
LRRCC1 Ac. tub.
Human
d
LRRCC1?
U-ExM z-stack
3D reconstruction
Θ analysis
LRRCC1 localization in procentrioles?
Procentriole position/ centriolar LRRCC1?
RPE1
HEK 293
LRRCC1 in procentrioles
Procentriole in distal view
CEN
42 %
LRRCC1
12 %
PRO
7 %
39 %
N = 69
p = 0.0016
Procentriole in distal view
CEN
34%
LRRCC1
17 %
PRO
25 %
24 %
N = 91
NS
Frequency of LRRCC1 localization
50 %
40 %
30 %
20 %
10 %
0 %
Procentriole position
Centriole in distal view
32 %
PRO
LRRCC1
32 %
CEN
9 %
27 %
N = 87
p = 0.0468
Centriole in distal view
34 %
PRO
LRRCC1
31 %
CEN
7 %
28 %
N = 89
p = 0.0101
Frequency of procentriole localization
50 %
40 %
30 %
20 %
10 %
0 %

Figure 4

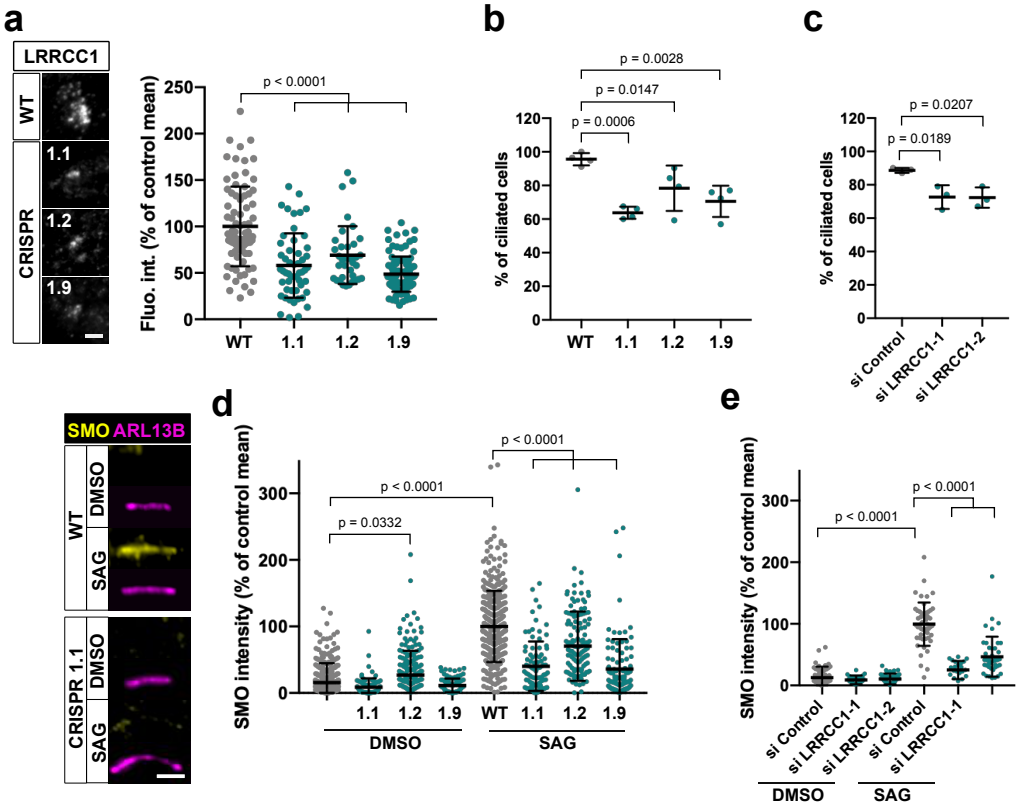
a
LRRCC1
WT
CRISPR
1.1
1.2
1.9
Fluo. int. (% of control mean)
p < 0.0001
WT 1.1 1.2 1.9
b
% of ciliated cells
p = 0.0028
p = 0.0147
p = 0.0006
WT 1.1 1.2 1.9
c
% of ciliated cells
p = 0.0207
p = 0.0189
si Control
si LRRCC1-1
si LRRCC1-2
SMO ARL13B
WT
DMSO
SAG
CRISPR 1.1
DMSO
SAG
d
SMO intensity (% of control mean)
p < 0.0001
p < 0.0001
p = 0.0332
1.1 1.2 1.9 WT 1.1 1.2 1.9
DMSO
SAG
e
SMO intensity (% of control mean)
p < 0.0001
p < 0.0001
si Control
si LRRCC1-1
si LRRCC1-2
si Control
si LRRCC1-1
DMSO
SAG

Figure 5

Gaudin *et al.*

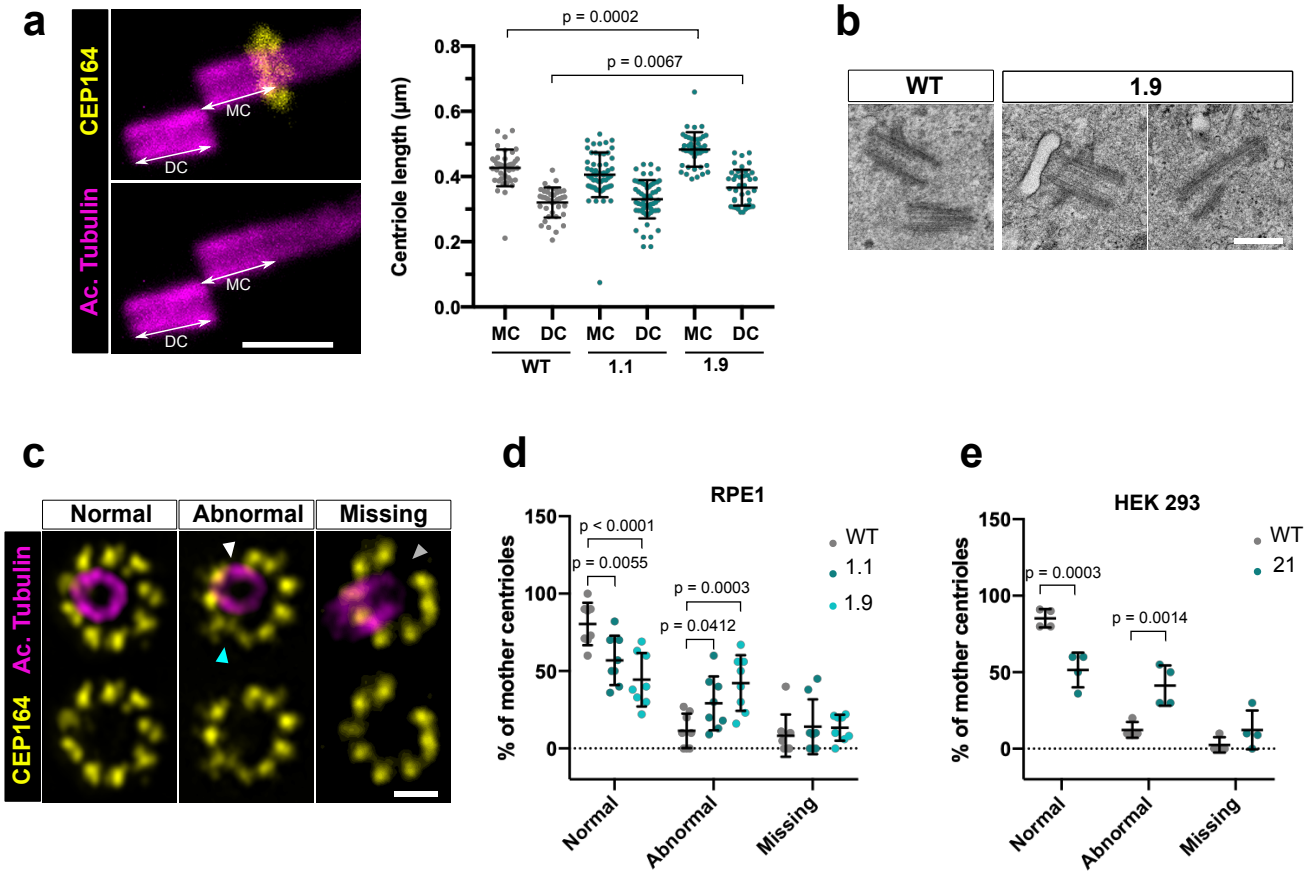

Figure 6

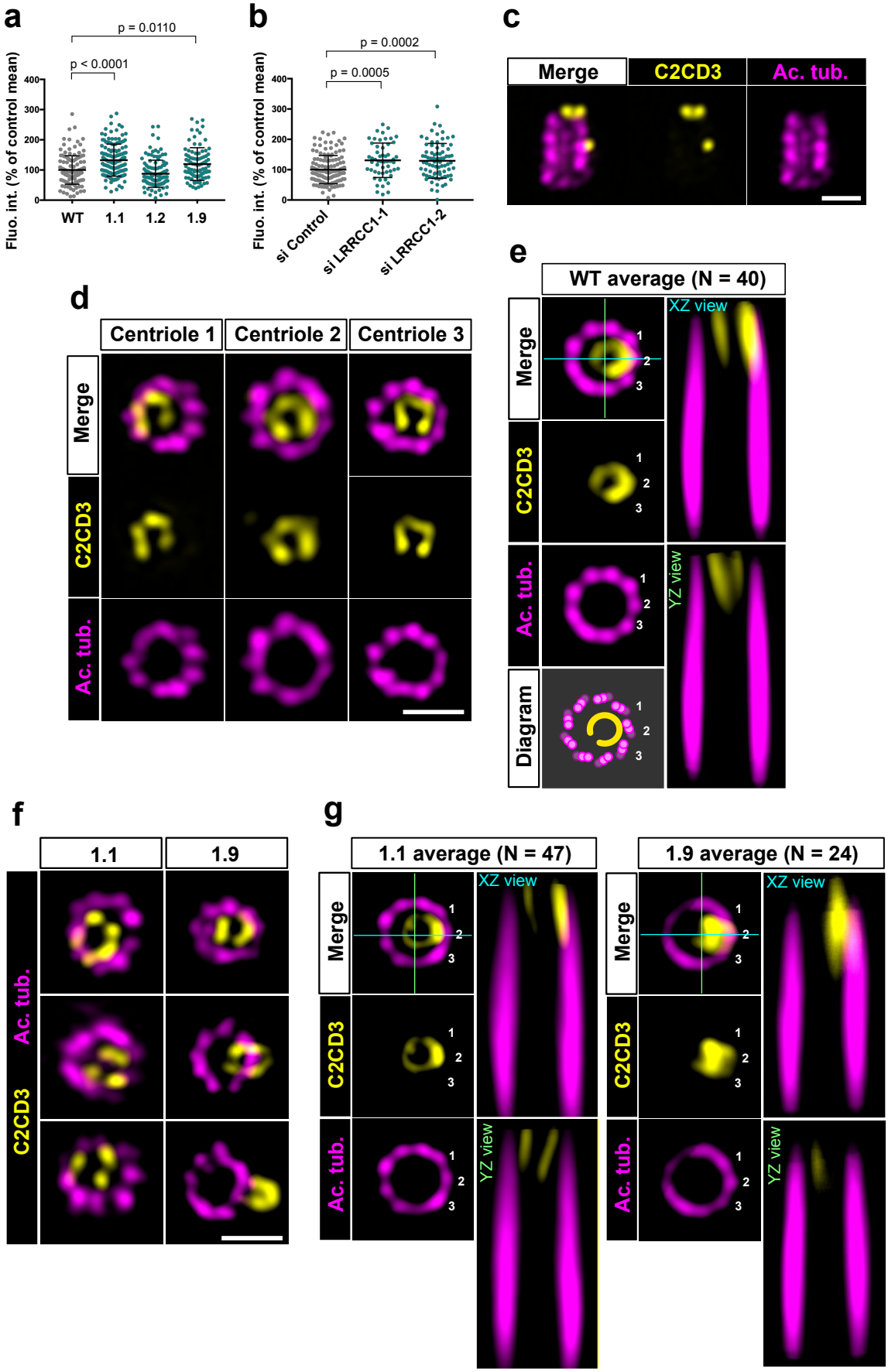
a
p = 0.0110
p < 0.0001
Fluo. int. (% of control mean)
400
300
200
100
0
WT
1.1
1.2
1.9
b
p = 0.0002
p = 0.0005
Fluo. int. (% of control mean)
si Control
si LRRCC1-1
si LRRCC1-2
c
Merge
C2CD3
Ac. tub.
d
Centriole 1
Centriole 2
Centriole 3
Merge
C2CD3
Ac. tub.
e
WT average (N = 40)
Merge
C2CD3
Ac. tub.
Diagram
XZ view
YZ view
1
2
3
f
1.1
1.9
Ac. tub.
C2CD3
g
1.1 average (N = 47)
1.9 average (N = 24)
Merge
C2CD3
Ac. tub.
XZ view
YZ view

Figure 7

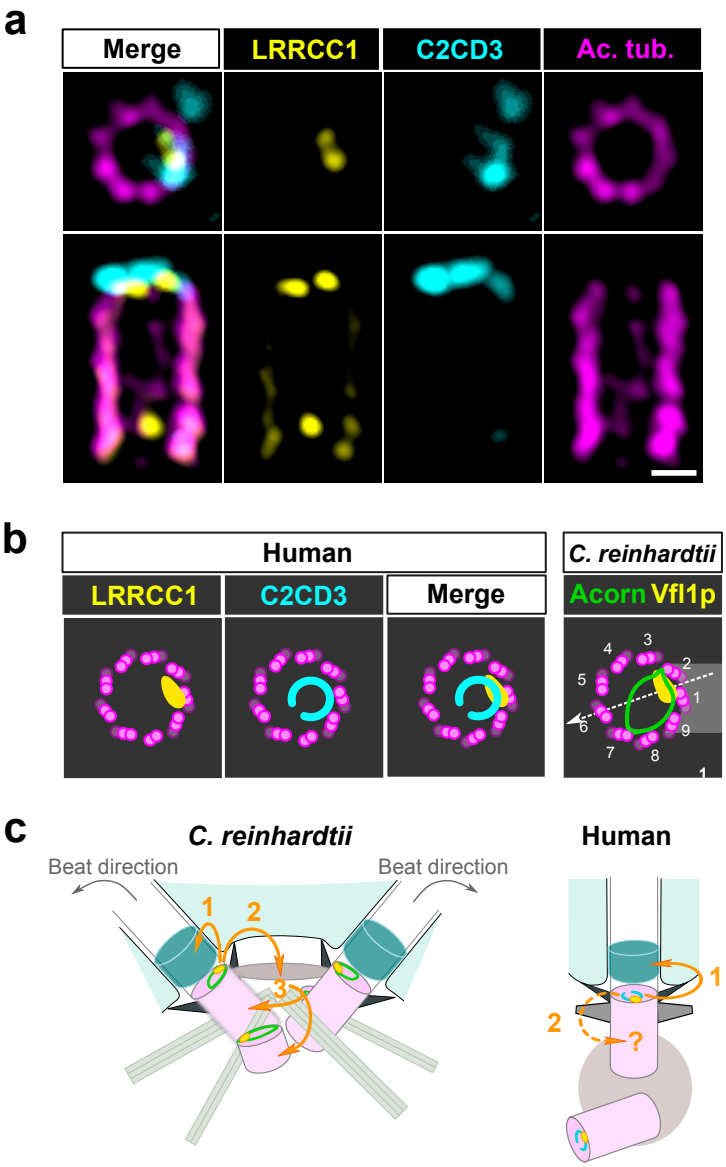
a
Merge
LRRCC1
C2CD3
Ac. tub.
b
Human
C. reinhardtii
LRRCC1
C2CD3
Merge
Acorn
Vfl1p
c
C. reinhardtii
Human
Beat direction
Beat direction
1
2
3
1
2
?